Journal of Computational Physics 229 (2010) 4613–4647

Contents lists available at ScienceDirect

Journal of Computational Physics

journal homepage: www.elsevier.com/locate/jcp

A robust numerical model for premixed flames with high density ratios based on new pressure correction and IMEX schemes

F. Paravento

Laboratory for Aero & Hydrodynamics, Delft University of Technology, The Netherlands

ARTICLE INFO

Article history:
Received 4 May 2009
Received in revised form 26 February 2010
Accepted 1 March 2010
Available online 6 March 2010

Keywords:
Premixed combustion
Low Mach number approximation
Level set
Implicit–explicit Runge–Kutta method
Immersed boundary method
Pressure correction

ABSTRACT

In this study we present a model for the interaction of premixed flames with obstacles in a channel flow. Although the flow equations are solved with Direct Numerical Simulation using a low Mach number approximation, the resolution used in the computation is limited (∼1 mm) hence the inner structure of the flame and the chemical scales are not solved. The species equations are substituted with a source term in the energy equation that simulates a one-step global reaction. A level set method is applied to track the position of the flame and its zero level is used to activate the source term in the energy equation only at the flame front. An immersed boundary method reproduces the geometry of the obstacles. The main contribution of the paper is represented by the proposed numerical approach: an IMEX (implicit–explicit) Runge–Kutta scheme is used for the time integration of the energy equation and a new pressure correction algorithm is introduced for the time integration of the momentum equations. The approach presented here allows to calculate flames which produce high density ratios between burnt and unburnt regions. The model is verified by simulating first simple solutions for one- and two-dimensional flames. At last, the experiments performed by Masri and Ibrahim with square and rectangular bodies are calculated.

1. Introduction

Masri et al. [1], Ibrahim et al. [2,38] and Hargrave et al. [3] performed experiments with obstacles in a channel where a premixed flame was ignited. They found that the shape of the obstacles and their blockage ratio have influence on the flame speed and on the overpressure. The flame starts as a laminar front which generates a flow in the channel. Shear flow is produced by the obstacles and the level of turbulence starts to rise. As a consequence the flame is wrinkled and its surface area increases. The propagation speed is proportional to the flame surface and increases. It is clear that the possibility to predict such interaction can help to improve the design of complex systems like for instance, industrial plants and to reduce the risk in case of deflagrations.

The aim of this work is mostly numerical with the scope of proposing a stable algorithm for high density ratio flames like in the case of Masri et al. experiments. Simplifications are adopted to overcome the limitations represented by the complex chemical mechanisms of the premixed combustion process. The proposed model is able to avoid the numerical instabilities that could arise during the computation of premixed flames with high density rations and heat transfer with obstacles. Our computations use DNS (Direct Numerical Simulation) for the resolution of the flow equations although due to the low resolution adopted (∼1 mm) the smallest flame/vortex interactions will probably not be captured. While the inner structure of

E-mail address: fabio.paravento@gmail.com

0021-9991/$ - see front matter © 2010 Elsevier Inc. All rights reserved.
doi:10.1016/j.jcp.2010.03.002

the flame and the chemical scales are not solved, the reacting part (energy equation with source term) is modeled with a level set approach (*G*-equation, [4]). This approach removes the need for solving the detailed chemistry and does not require a model for the turbulence. The *G*-equation does not interact directly with the flow, it simply tracks the position of the flame and its zero level location is used to activate the source term in the energy equation at that location where the flame front is located for each particular time.

This work is organized in three main sections. In the first section the governing equations are introduced, in the second one the numerical methods for their integration are presented together with a stability analysis. In the third section results for simple cases and for the interaction of a premixed flame with obstacles are presented and discussed. In particular, we reproduce the experiment performed by Ibrahim [2,38] in which the speed of the flame front was measured.

1.1. The set of equations

A system of equations that allows for large heat release, large temperature and density variations and substantial interaction with the hydrodynamic flow field including the effects of the turbulence is required. A low Mach number approximation is suitable in such a case with remarkable advantages regarding the implementation because we do not have to resolve the acoustic oscillations and the set of equations is similar to the incompressible case but the density may vary due to heat release [5–7].

Following the asymptotic derivation given by Buckmaster and Ludford [41] or recently found also in Müller [8], it can be shown [33] that the non-dimensional set of continuity, momentum and temperature equations (with source term $\dot{\omega}$) in low Mach number approximation is

$$\frac{\partial \rho}{\partial t} + \nabla \cdot (\rho u) = 0 \tag{1}$$

$$\frac{\partial \rho u}{\partial t} + \nabla \cdot (\rho u u) = -\nabla p + \frac{1}{Re} \nabla \cdot \tau \tag{2}$$

$$\rho \frac{\partial T}{\partial t} + \rho u \nabla \cdot T = \frac{1}{Re\,Pr} \nabla \cdot (\lambda \nabla T) + \rho \dot{\omega} \tag{3}$$

With ρ being the density, u the velocity, p the dynamic pressure, T the temperature, λ the thermal conductivity (taken here constant and scaled such that it is equal to unity) and τ the Newtonian stress tensor. An equation of state for ideal gas is also used,

$$p_0 = \rho T \tag{4}$$

In this derivation the thermodynamic pressure p_0 has been assumed constant and the influence of gravity is neglected. Moreover the effect of viscous dissipation in the energy equation drops out as a result of the approximation.

The position of the flame is found by solving a level set equation whose variable G is defined as a distance function [4]. The *G*-equation describes the evolution of the front as a level set function that is continuous through the flame front [44]. An implicit representation of the instantaneous flame surface can be given as [44]

$$G(x_f, t) - G_0 = 0 \tag{5}$$

which defines the level set function G. Here, t is the time and x_f is the vector of the flame front location. Differentiating the previous equation with respect to time one obtains

$$\frac{\partial G}{\partial t} + \frac{dx_f}{dt} \cdot \nabla G = 0 \tag{6}$$

The flame front propagation speed is given by

$$\frac{dx_f}{dt} = u + s_l n \tag{7}$$

where u is the local flow velocity, s_l is the laminar burning speed and n is the flame normal defined to be directed into the unburned mixture and its expression is

$$n = -\frac{\nabla G}{|\nabla G|} \tag{8}$$

By imposing $|\nabla G| = 1$ (everywhere in the domain by a reinitialization procedure) this makes sure that the G values give always the distance form the zero level. The advantage of G being a distance function is that it is now not necessary to track the position of the flame front in order to determine the distance from the flame front at a certain point x since this distance now is given by $G(x) - G_0$ and if G_0 is assumed as origin of the coordinates then it is given by $G(x)$.

The laminar burning speed, s_l may be different from the unstrained laminar burning speed (let us call it s_L^0) because of the shape of the flame that changes during the propagation forming points where the speed is higher than s_L^0 due to the effect of the flame stretch.

A relation for s_l was derived in general form by [43] and in linear version by Pelce and Calvin [9]. In this study we use the flame speed relation proposed by Piana et al. [10] that takes into account the effect of the density variation between the burnt and the fresh regions by the term $\frac{\rho_u}{\rho}$ with ρ_u being the density of the unburnt mixture and ρ the local density:

$$s_l = [s_L^0 - s_L^0 L_M \nabla \cdot n + L_M n \cdot (\nabla u) \cdot n] \frac{\rho_u}{\rho} \tag{9}$$

L_M is the Markstein length. s_L^0 is the laminar burning speed which is the characteristic propagation speed of a non-stretched flame. This quantity depends only on the composition of the mixture. In Eq. (9) the second and the third terms on the right hand side are called the curvature and the strain terms respectively.

From the combination of the previous relations the instantaneous G-equation reads

$$\frac{\partial G}{\partial t} + u \cdot \nabla G = s_l |\nabla G| \tag{10}$$

The G-equation can be re-casted in pure advection form (as shown in Appendix A) for numerical integration.

The source is modeled as function of the G variable. This means that energy is released only at the position of the flame. A similar approach was first proposed by Piana [10,37]. We use the following relation for the source

$$\dot{\omega}(G) = \tau_h \left(\frac{T_f}{T_u} - T \right) \frac{s_l}{\delta} \exp\left(-\frac{G^2}{2\delta^2} \right) \tag{11}$$

where T_u is the temperature of the unburnt gas, T_f is the adiabatic flame temperature, T is the local temperature, G indicates the level set variable, τ_h is the heat release parameter defined as $\tau_h = \frac{T_f - T_u}{T_u}$ and δ is a numerical thickness which we interpret as the diffusive flame thickness. The diffusive thickness δ is usually defined in terms of unburned mixture properties [11,14],

$$\delta \sim \lambda / c_p \rho_u s_l \tag{12}$$

The Markstein length is of the order of the diffusive flame thickness δ and, assuming Lewis number equal to one, it can be evaluated with [12]

$$L_M = \frac{T_f}{T_f - T_u} \ln\left(\frac{T_f}{T_u} \right) \delta \tag{13}$$

Another important quantity is the thermal flame thicknesses, δ_f defined as

$$\delta_f = \frac{T_f - T_u}{\max\left(\left| \frac{dT}{dn} \right| \right)} \tag{14}$$

where $\frac{dT}{dn}$ is the derivative of the temperature in the normal direction of the flame front.

δ is smaller than δ_f, usually by a factor of order 5 [11], and a correlation can be found between these two quantities [13]. In this study δ_f is evaluated with a first flame computation. Then, we optimize δ and L_M according to the profile of δ_f. This is not strictly necessary and has been done because an improvement in the prediction of the flame speed has been found of about 5–10% when compared with experimental data.

1.2. The immersed boundary method (IBM)

With an IBM we can simulate a geometry by adding forces within the grid. In this way the grid does not depend on the geometry being solved and it can be simple Cartesian. We use the method illustrated by Breugem and Boersma [15] with an extension for the simulation of the heat transfer at the body walls [16]. Because the geometry consists of square or rectangular bodies in a flow we can align the obstacles with the sides of the grid cells where the perpendicular velocity components are defined. In this way the non-penetration condition for the velocity can be applied very accurately.

The algorithm for the integration of the Navier–Stokes equations (pressure correction algorithm) contains a Poisson equation that must be solved. For an arbitrary grid this can be done with an iterative solver but the computational time can be quite high for complex geometries. Based on the separable nature of the Poisson equation so-called "Fast" Poisson solvers exist for simple grid cases. The IBM allows for complex geometries while still dealing with a simple Poisson problem. To simulate the boundaries an extra force is inserted into the momentum equations,

$$\frac{\partial \rho u}{\partial t} + \nabla \cdot (\rho u u) = -\nabla p + \frac{1}{Re} \nabla \cdot \tau + f \tag{15}$$

where f represents the body force. In the Breugem and Boersma's IBM approach the force f is calculated in such a way that no-slip conditions at the boundary apply. In addition, the non-penetration condition at the walls is enforced by imposing the normal components of the mass flux and the related velocity to be zero. All details can be found in [16]. Here we want to recall from [16] that it is very important to adopt the correct IBM temperature treatment when an heat flux (zero in adiabatic case) is considered from the surface of an obstacle.

When temperature differences are introduced, (for example in the case of interaction flame/flow/body), the heat flux between boundaries and the flow can be well represented with a procedure similar to the stress replacement method for the momentum equation. In practice, the heat flux on the walls of an obstacle must be adjusted by modifying the diffusion and convective terms in the temperature equation at the inner side of body boundary in such a way to force the correct flux at the boundary.

To conclude this section it appears useful to mention that the boundary condition for G when the front reaches an obstacle is $\nabla G = 0$ hence we assume that the level set sticks to the obstacle once this is passed.

2. A model for premixed flames with high density ratios

By using a level set-based model to mimic the chemistry there are no species equations to be solved and the computational effort is considerably reduced. However, numerical difficulties arise when one has to model flames which generate high variations of density between the fresh mixture and the burnt gases. This is because steep gradients of flow quantities and temperature values appear due to the fast heat release. In particular, the numerical scheme for the governing equations must be able to handle the strong density gradients. Two main issues need to be addressed. One is the time integration of the temperature equation with steep source term. The other issue is the calculation of the time derivative of the density that is used to build the Poisson equation in the pressure correction algorithm.

There exist G-equation methods where no heat transfer is considered and no source term has to be integrated. One of these methods is the pure G-equation model proposed by Treurniet [17]. In this model there is no energy equation to be solved and therefore no source needs to be ignited. Instead, smooth temperature and density profiles are chosen from the beginning of the calculation. With the pure G-equation approach high density ratios between burnt and unburnt regions can be easily handled but not heat transfer with obstacles. In our model, the momentum equation and the energy (temperature) equation are coupled by the equation of state. The source term in the energy equation is a function of the level set variable G. The spatial discretization of the momentum and the continuity equations is done with a second order finite volume method [23] and the time integration is based on a third order Adams–Bashforth scheme (AB3). For the G-equation the space discretization uses a local third order WENO scheme [28], while for its time integration AB3 is used. The same WENO scheme is used for the spatial discretization of the convective term in the temperature equation while the discretization of the diffusive term is carried out using a central difference scheme. An IMEX scheme ('implicit' integration of the source and 'explicit' integration of the advection–diffusion terms) is used for the time integration of the temperature equation. The IMEX scheme used in this approach was proposed by Pareschi [20]. Implicit–explicit schemes represent a well known numerical technique but they have only recently started to be applied to combustion problems and are under continuous development [18].

2.1. The integration of the energy equation with source term

The temperature equation is

$$\frac{\partial T}{\partial t} + u\nabla \cdot T = \frac{1}{\rho}\frac{1}{RePr}\nabla \cdot (\lambda \nabla T) + \dot{\omega} \tag{16}$$

with source term $\dot{\omega}$ defined by (11). The source can be re-written as

$$\dot{\omega} = \frac{s_l}{\delta}\tau_h\left(\frac{T_f}{T_u} - T\right)\exp\left(-\frac{G^2}{2\delta^2}\right) = \frac{1}{\epsilon}S \tag{17}$$

with $\epsilon = \frac{\delta}{s_l}$ and $S = \tau_h\left(\frac{T_f}{T_u} - T\right)\exp\left(-\frac{G^2}{2\delta^2}\right)$. Now, let us represent the convective and diffusive terms as

$$R(T) = -u\nabla \cdot T + \frac{1}{\rho}\frac{1}{RePr}\nabla \cdot (\lambda \nabla T) \tag{18}$$

Then the temperature equation can be written

$$\frac{\partial T}{\partial t} = R(T) + \frac{S(T)}{\epsilon} \tag{19}$$

ϵ is a parameter which controls the magnitude of the source term. It represents the time scale of the source. Eq. (19) can be seen as a system with relaxation term $(\frac{S}{\epsilon})$. Methods for such systems have been an active area of research in the past [19] for applications in combustion, multi-phase flows and rarefied gas dynamics.

We integrate the temperature in time with the IMEX scheme proposed by Pareschi [20]. Pareschi's scheme is a so-called time split scheme. Two implicit steps for the integration of the source, S, advance the temperature to two intermediate values T^* and T^{**} while the other terms, $R(T)$, are integrated in three steps with intermediate values for the temperature $T^{(1)}$ and $T^{(2)}$:

$$T^{*} = T^{n} + \frac{\Delta t}{(2\alpha - 1)} \frac{(\alpha - 1)}{\varepsilon} S(T^{*}) \tag{20}$$

$$T^{(1)} = T^{n} + \Delta t \alpha R(T^{*}) \tag{21}$$

$$T^{**} = T^{(1)} + \frac{\Delta t}{\varepsilon}[\xi S(T^{*}) + (1 - \xi) S(T^{**})] \tag{22}$$

$$T^{(2)} = T^{n} + \frac{\Delta t}{2\alpha}[(2\alpha - 1) R(T^{*}) + R(T^{**})] \tag{23}$$

$$T^{n+1} = T^{(2)} + \frac{\Delta t}{2\alpha\varepsilon}[(2\alpha - 1) S(T^{*}) + S(T^{**})] \tag{24}$$

The coefficients $\alpha = 5/3$ and $\xi = 7/10$ result from a stability analysis performed by Pareschi [20]. For the implicit steps we use one iteration per time step.

2.1.1. Comparison of the IMEX scheme with an explicit scheme

In this section we show that the IMEX scheme allows for a larger time step than a conventional explicit scheme. Let us consider also an explicit method (AB3-EF) for the time integration of the energy equation, consisting of a third order Adams–Bashforth scheme for the advection and the diffusion terms (represented by R) and an Euler forward scheme for the source ($\dot{\omega}$):

$$T^{n+1} - T^{n} = \frac{1}{12}[23R^{n} - 16R^{n-1} + 5R^{n-2}]\Delta t + \dot{\omega}^{n}\Delta t \tag{25}$$

To compare the two schemes we consider a simplified 1D model: an advection–diffusion equation with a linear source term $S(T)$. Advection velocity (U) and diffusion coefficients (D) are considered constant.

2.1.2. Advection–diffusion-source test

In this case we have,

$$\frac{\partial T}{\partial t} + U\frac{\partial T}{\partial x} = D\frac{\partial^{2} T}{\partial x^{2}} + S(T) \tag{26}$$

By using a change of variables, $x' = x - Ut$ and $t = t'$, and applying the chain rule, the previous equation can be written in a diffusive form,

$$\frac{\partial T}{\partial t'} = D\frac{\partial^{2} T}{\partial x'^{2}} + S(T) \tag{27}$$

To simplify the problem the source is taken as $S(T) = \frac{T}{\epsilon}$. This diffusion equation with linear source has an exact analytical solution whose form is a sum of trigonometric functions weighted with coefficients depending on the initial and boundary conditions:

$$\begin{cases} T(x', t) = \sum_{n=1}^{\infty} D_n e^{-\lambda_n t} \sin\frac{n\pi x'}{L} \\ D_n = \frac{2}{L}\int_0^L T_0 \sin\frac{2\pi x'}{L} dx' \end{cases}$$

with $\lambda_n = \frac{Dn^2\pi^2}{L^2} - \frac{s_l}{\delta}$ and $T(0, x')$ initial condition. As boundary conditions we use $T(t, x' = 0) = T(t, x' = L) = 0$ with $L = 0.15$ being the size of the one-dimensional domain and $N = 100$ the number of points. These parameters give L/N the same order of magnitude as dx used in the 3D computations discussed later in Section 3.

As initial condition we consider an impulsive temperature distribution given by

$$T(0, x') = \frac{s_l}{\delta} \exp\left(-\frac{(x' - L/2)^2}{2\delta^2}\right) \tag{28}$$

with $\delta = 0.0004$ and $s_l = (\epsilon^{-1})\delta$. As discussed in chapter two, δ is interpreted as the diffusion flame thickness which is smaller than the thermal flame thickness. δ is chosen such that the full width at half maximum of the distribution is of the order of a grid cell size. By increasing the quantity ϵ^{-1} the spatial sharpness of the initial distribution increases. In this test we use $\epsilon = 0.001$ (which is consistent with the value used in the case of 3D simulations where $s_l = 0.4$).

Eq. (26) is solved numerically with IMEX and AB3-EF schemes. An absolute error can be defined between the numerical and the analytical solutions:

$$err = \frac{1}{N}\sum_{1}^{N} |\phi - \phi_{an}|$$

where ϕ is the numerical solution and ϕ_{an} the analytical solution.

In Table 1 the errors of the two schemes are shown for the case $U = 1$ and $D = 1$. The integration is performed from time zero till $t = 10^{-5}$ with different time steps. In Table 2 the same quantities are shown for the case $U = 1$ and $D = 0.01$ and the

Table 1
Absolute error and maximum values for different time steps. Grid resolution 100 points. $D = 1,\ U = 1$ and $\epsilon = 0.001$. Integration until time = 10^{-5}.

Number of points	Δt	Error IMEX	Error AB3-EF	maxval(T) IMEX	maxval(T) AB3-EF	maxval(T) exact
100	10^{-8}	0.251	0.249	259.343	259.281	255.878
100	10^{-7}	0.252	0.222	259.347	258.722	255.878
100	10^{-6}	0.379	311197.969	261.400	–	255.878

Table 2
Absolute error and maximum values for different time steps. Grid resolution 100 points. $D = 0.01,\ U = 1$ and $\epsilon = 0.001$. Integration until time = 10^{-3}.

Number of points	Δt	Error IMEX	Error AB3-EF	maxval(T) IMEX	maxval(T) AB3-EF	maxval(T) exact
100	10^{-6}	9.139	9.135	696.288	696.043	688.627
100	10^{-5}	9.137	9.095	695.579	692.936	688.627
100	10^{-4}	8.765	450379.812	684.129	–	688.627

Table 3
Absolute error for different grid resolutions. $U = 1,\ D = 0.01$ and $\epsilon = 0.001$. Integration for 1000 time steps. $\Delta t = 10^{-9}$.

Number of points	Δx	Error IMEX	Error AB3-EF
25	0.006	649.7161	649.7185
50	0.003	96.7029	96.7029
100	0.0015	20.9853	20.9854
200	0.00075	3.7240	3.7242
400	0.000375	0.3338	0.3339

integration goes from zero to $t = 10^{-3}$ for different time steps. It can be seen that the AB3-EF scheme diverges when the time step increases to 10^{-6} and 10^{-4} respectively.[1]

Now, let us consider different spatial resolutions: 25, 50, 100, 200 and 400 points. We consider $U = 1,\ D = 0.01$ and $\epsilon = 0.001$. Moreover we define $\delta = \frac{\Delta x}{3}$ for each resolution. This is because a similar formulation for the diffusive flame thickness will be introduced later in this paper for the case of realistic combustion simulations. A small time step is chosen ($\Delta t = 10^{-9}$) and the equations are integrated for 1000 time steps. In Table 3 are reported the errors of IMEX and AB3-EF schemes. With the refinement of the grid the errors reduce drastically. In Fig. 1 we plot the L2 integral Root Mean Square (RMS) norm error for the IMEX scheme as function of the number of grid points. The solution is essentially accurate to second order.

2.1.3. Stability analysis

A numerical method whose vector solution at time n is Y_n, is said absolute stable if there exists a matrix C of elements c_n such that

$$|Y_{n+1}| \leqslant C|Y_n|$$

with

$$0 < c_n < 1 \quad \forall n$$

For simple Cauchy problems (like $y' = By,\ y(0) = y_0$ with $y \in R^m$ and $B \in R^{m\times m}$) the matrix C can be easily calculated. Then the radius of the matrix C of absolute stability can be calculated and the stability region can be represented (more details can be found in Lambert [22] or Hirsch [23]). However, as pointed out by Pareschi and Russo [24], for a generic linear system $y' = B_1 y + B_2 y$ if we want to integrate in time (for example with IMEX) the term $B_1 y$ explicitly and the term $B_2 y$ implicitly, then the stability matrix depends on the two matrices B_1 and B_2 and not only on their eigenvalues because in general these matrices do not have the same eigenvectors and they cannot be diagonalized simultaneously.

For simplicity, let us consider the diffusion equation with linear source,

$$\frac{\partial T}{\partial t} = D\frac{\partial^2 T}{\partial x^2} + \frac{T}{\epsilon} \tag{29}$$

We apply to this equation the Von Neumann analysis to derive the characteristic stability polynomial for the AB3-EF and the IMEX schemes. The fact that we remove the advection for the second case allows us to derive polynomials without complex coefficients. This simplifies the analysis. By considering periodicity in space we apply a Fourier transformation to separate

[1] It is worth to mention here that we have also performed tests with another scheme based on AB3 for both the diffusive and the source terms. Also in this case we noted exploding calculations.

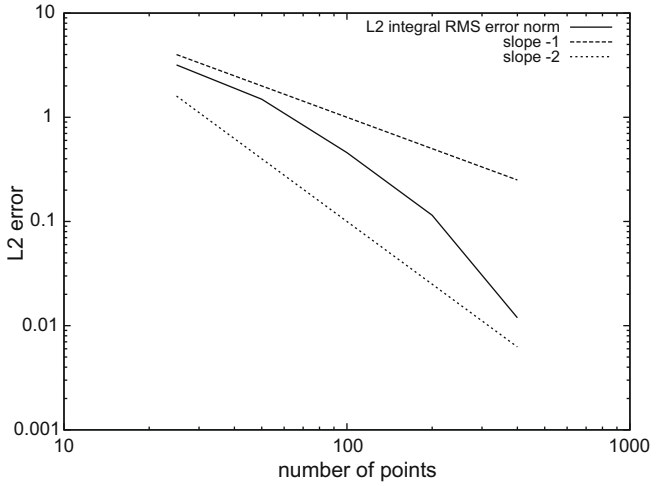

Fig. 1. The L2 (RMS) norm error for the IMEX scheme is shown as function of the grid resolution. The solution is essentially accurate to second order.

the space from the time dependence by using the substitution $T_i^n = Y_n e^{ji\theta}$ where n indicates the number of time step, i is an integer and indicates the space position, $j = \sqrt{-1}$ is the imaginary unit and $\theta \in [0, 2\pi]$. By using central differences we can discretize Eq. (29) for AB3-EF scheme as:

$$\frac{(Y_{n+1} - Y_n)e^{ji\theta}}{\Delta t} = \frac{D}{\Delta x^2}\left(\frac{23}{12}R^n - \frac{16}{12}R^{n-1} + \frac{5}{12}R^{n-2}\right) + \frac{Y_n e^{ji\theta}}{\epsilon}$$

with

$$R^n = Y_n e^{j(i+1)\theta} - 2Y_n e^{ji\theta} + Y_n e^{j(i-1)\theta}$$

By using the relation $e^{j\theta} + e^{-j\theta} = 2\cos\theta$ and dividing by $e^{ji\theta}$ we find

$$\frac{Y_{n+1} - Y_n}{\Delta t} = \frac{2D}{\Delta x^2}(\cos\theta - 1)\left(\frac{23}{12}Y_n - \frac{16}{12}Y_{n-1} + \frac{5}{12}Y_{n-2}\right) + \frac{Y_n}{\epsilon}$$

Further, by considering $\left|\frac{Y_{n+1}}{Y_n}\right| = \left|\frac{Y_n}{Y_{n-1}}\right| = \left|\frac{Y_{n-1}}{Y_{n-2}}\right| = \left|\frac{Y_{n-2}}{Y_{n-3}}\right| = r$ we can write

$$\frac{1}{\Delta t}(r^2 - r) = \frac{2D}{\Delta x^2}(\cos\theta - 1)\left(\frac{23}{12}r - \frac{16}{12} + \frac{5}{12}\frac{1}{r}\right) + \frac{r}{\epsilon}$$

By rearranging the terms in the last relation the stability polynomial for AB3-EF is

$$r^3 - r^2\left[1 + \frac{23}{12}\frac{2D}{\Delta x^2}(\cos\theta - 1)\Delta t + \frac{\Delta t}{\epsilon}\right] + r\left[\frac{16}{12}\frac{2D}{\Delta x^2}(\cos\theta - 1)\Delta t\right] - \left[\frac{5}{12}\frac{2D}{\Delta x^2}(\cos\theta - 1)\Delta t\right] = 0 \tag{30}$$

The scheme is stable if its polynomial has roots, r, such that $|r| \leqslant 1$.

Applying the same Von Neumann procedure we can find the stability polynomial of the IMEX scheme with root r such that

$$\begin{aligned} r = \frac{Y_{n+1}}{Y_n} &= 1 + \frac{\Delta t(2\alpha - 1)/(2\alpha)}{\left(1 - \frac{(\alpha-1)\Delta t}{\epsilon(2\alpha-1)}\right)}\frac{2D}{\Delta x^2}(\cos\theta - 1) \\ &+ \frac{\Delta t D}{2\alpha\Delta x^2}\left[\frac{2\cos\theta + \frac{\Delta t\alpha}{\left(1-\frac{(\alpha-1)\Delta t}{\epsilon(2\alpha-1)}\right)}\frac{2D}{\Delta x^2}(1 + \cos 2\theta - 2\cos\theta)\frac{\Delta t\xi}{\epsilon}\frac{2\cos\theta}{\left(1-\frac{(\alpha-1)\Delta t}{\epsilon(2\alpha-1)}\right)}}{1 - \frac{(1-\xi)\Delta t}{\epsilon}}\right] \\ &- \frac{\Delta t D}{\alpha\Delta x^2}\left[\frac{1 + \frac{\Delta t\alpha}{(1-\frac{(\alpha-1)\Delta t}{\epsilon(2\alpha-1)})}\frac{2D}{\Delta x^2}(\cos\theta - 1) + \frac{\Delta t\xi}{\epsilon}\frac{1}{\left(1-\frac{(\alpha-1)\Delta t}{\epsilon(2\alpha-1)}\right)}}{1 - \frac{(1-\xi)\Delta t}{\epsilon}}\right] + \frac{\Delta t(2\alpha - 1)}{2\alpha\epsilon}\left[\frac{1}{\left(1 - \frac{(\alpha-1)\Delta t}{\epsilon(2\alpha-1)}\right)}\right] \\ &+ \frac{\frac{\Delta t}{2\alpha\epsilon}}{1 - \frac{(1-\xi)\Delta t}{\epsilon}}\left[1 + \frac{\Delta t\alpha}{\left(1 - \frac{(\alpha-1)\Delta t}{\epsilon(2\alpha-1)}\right)}\frac{2D}{\Delta x^2}(\cos\theta - 1) + \frac{\Delta t\xi}{\epsilon}\frac{1}{\left(1 - \frac{(\alpha-1)\Delta t}{\epsilon(2\alpha-1)}\right)}\right] \end{aligned} \tag{31}$$

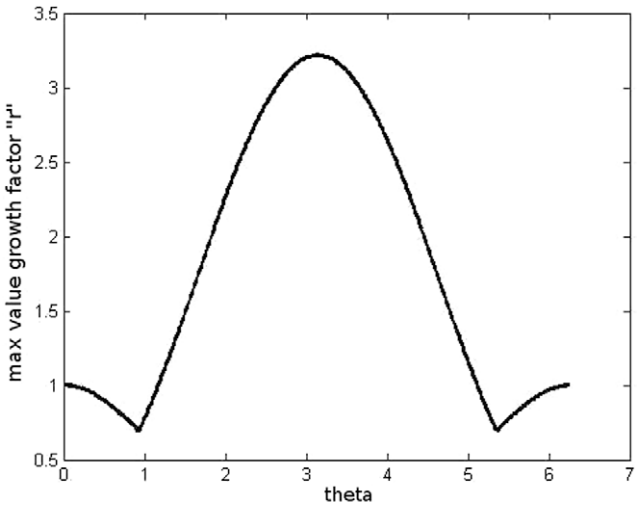

Fig. 2. The advection–diffusion equation with source term is solved with AB3-EF and IMEX schemes for the case with $D = 1$, $\epsilon = 0.001$ and $\Delta t = 10^{-6}$. The error growth factor for AB3-EF is larger than unity meaning an unstable behaviour.

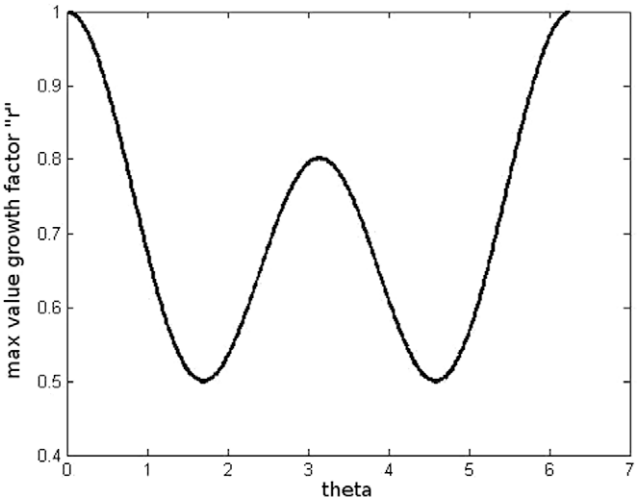

Fig. 3. The advection–diffusion equation with source term is solved with AB3-EF and IMEX schemes for the case with $D = 1$, $\epsilon = 0.001$ and $\Delta t = 10^{-6}$. The error growth factor for IMEX is smaller than unity.

Now, let us consider the parameters used for the runs in Tables 1 and 2 referring to the case when AB3-EF scheme fails. In the first case we considered $D = 1$, $\epsilon = 0.001$ and $\Delta t = 10^{-6}$, while in the second case the values were $D = 0.01$, $\epsilon = 0.001$ and $\Delta t = 10^{-4}$. For these two cases the maximum root r (that can be seen as growth factor for the numerical error) of the stability polynomials for AB3-EF and IMEX schemes are plotted versus θ (Figs. 2–5). In both cases only the IMEX scheme satisfies the stability condition $|r| \leqslant 1$.

In the particular case shown in Figs. 2 and 3 (the same applies to the case in Figs. 4 and 5), the maximum value of the growth factor curve for the AB3-EF scheme is about 3.2. If now we re-run this case with a time step 3.2 times smaller than in the first run we obtain a growth factor curve which is almost entirely in the stable region (Fig. 6). Therefore, for this case the IMEX scheme allows for a three times larger time step.

2.1.4. Sensitivity analysis

A sensitivity analysis for the IMEX scheme is shown below. Let us consider a stable case defined by the following parameters: $\Delta x = 0.015$, $D = 0.01$ and $\epsilon = 0.001$. The time step is $\Delta t = 10^{-6}$. This corresponds to the first case reported in Table 2. Now, if we vary one parameter at a time we can study how the growth factor changes, hence how the stability region of the scheme changes. In particular, if the area subtended between the unity straight line, $|r| = 1$, and the growth factor curve increases then the stability zone increases as well. In Fig. 7 D has values 0.01, 0.02 and 0.04. The stability region increases when

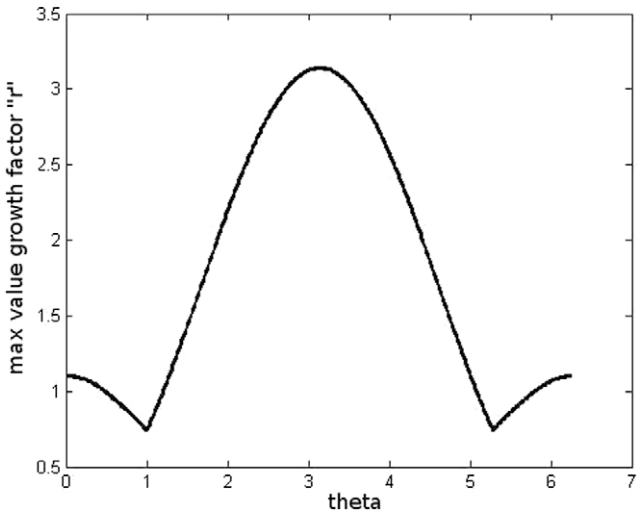

Fig. 4. The advection–diffusion equation with source term is solved with AB3-EF and IMEX schemes for the case with $D = 0.01$, $\epsilon = 0.001$ and $\Delta t = 10^{-4}$. The error growth factor for AB3-EF is larger than unity meaning an unstable behaviour.

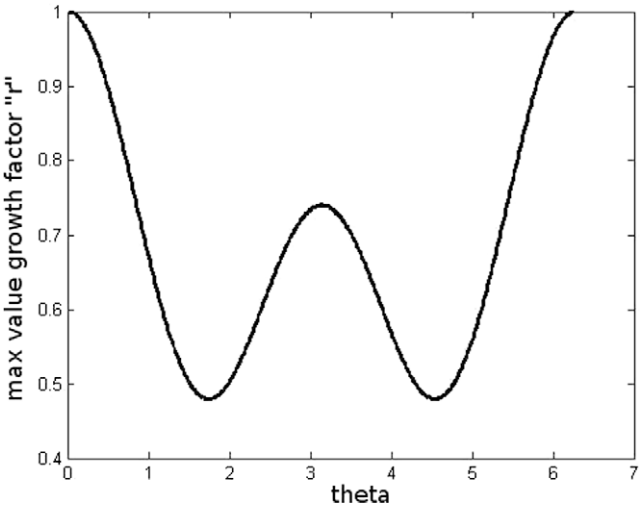

Fig. 5. The advection–diffusion equation with source term is solved with AB3-EF and IMEX schemes for the case with $D = 0.01$, $\epsilon = 0.001$ and $\Delta t = 10^{-4}$. The error growth factor for IMEX is smaller than unity.

D increases. In Fig. 8 Δx varies with values 0.001, 0.0015 and 0.002. In this case the stability region decreases when the grid gets coarser. In Fig. 9 we vary ϵ with values 0.0005, 0.001 and 0.002. In this last case also Δx has to change according to ϵ because we have defined $\delta = \Delta x/3 = s_l\epsilon$ therefore, in order to have a constant flame speed s_l, we use $\Delta x = 3s_l\epsilon$. We note that when ϵ decreases the stability region increases its area.

Because a general stability theory for IMEX schemes is not available yet, the sensitivity analysis shown here is only meant to give an idea of the influence of different parameters on the scheme without pretending to be exhaustive.

2.2. The new pressure correction algorithm

The pressure correction scheme in its original formulation, was first introduced by Chorin [26]. In case of constant density it is stable but it fails when a flow with sharp variable density is considered and the density ratio is high [27]. In this section we propose a pressure correction scheme that, in combination with the integration of the temperature equation introduced above, represents a suitable model for combustion with high density ratios. Then, the new algorithm is compared with a scheme derived from the pressure correction used by Treurniet [17]. Let us call this last scheme ‘classic’ to distinguish it from

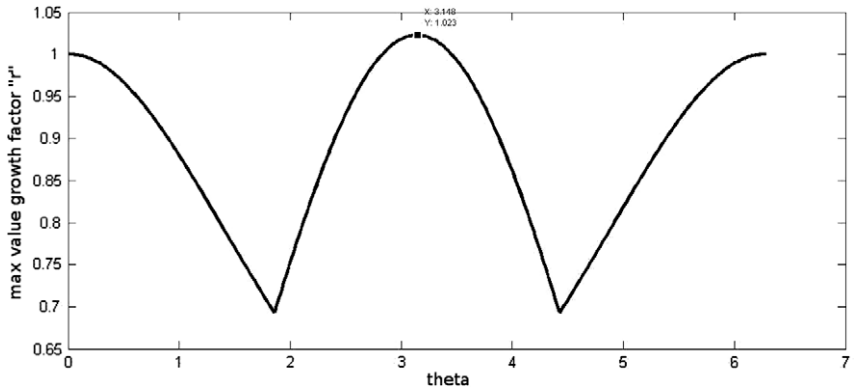

Fig. 6. Growth factor curve for the AB3-EF scheme when the computational time step is reduced about 3 times with respect to the IMEX scheme. The other parameters (D and ϵ) are the same like in the case shown in Fig. 2. In this case the AB3-EF scheme needs a time step three times smaller than for IMEX scheme in order to be stable.

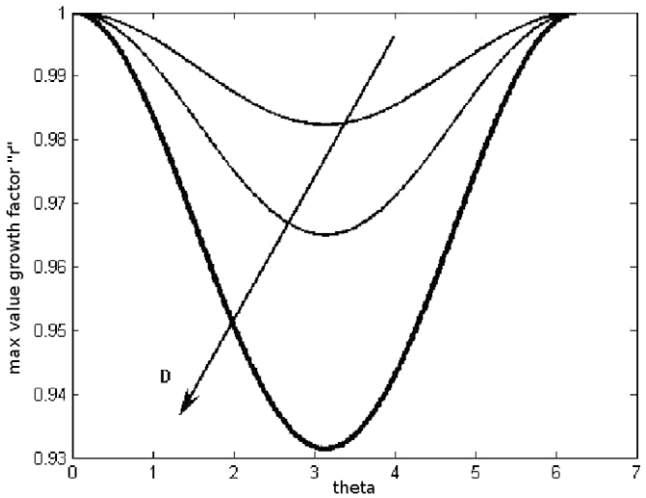

Fig. 7. Behaviour of the error growth factor for IMEX scheme when the diffusion parameter D has values 0.001, 0.002 and 0.004. The other parameters are $\Delta x = 0.015$ and $\epsilon = 0.001$. The time step is taken $\Delta t = 10^{-6}$. The direction of the arrow indicates increasing value of D.

our algorithm.[2] The main differences between our algorithm and the one used by Treurniet are the way the time derivative and the update of the density are computed. Now we describe the details of our scheme. Let us consider all quantities at time n (at the beginning of the calculation ($n = 0$) if quantities at times $n - 1$ and $n - 2$ are required, these are set equal to their values at time $n = 0$). At first the temperature is advanced to an intermediate value $\widehat{T}^{n+1}$ with the time integration based on IMEX scheme. Then, the quantity

$$\widehat{\frac{\partial T}{\partial t}}_{n+1} = \frac{\widehat{T}^{n+1} - T^n}{\Delta t} \tag{32}$$

is calculated. Further, the equation of state is used to compute

$$\widehat{\frac{\partial \rho}{\partial t}}_{n+1} = -\frac{P_0}{(\widehat{T}^{n+1})^2}\left(\widehat{\frac{\partial T}{\partial t}}_{n+1}\right) \tag{33}$$

[2] Treurniet [17] implemented the pressure correction in a predictor–corrector fashion (similar to the approach of Najm [21]). The predictor and the corrector parts of the algorithm have the same structure but they differ for the time integration of the momentum (second order Adam Bashforth for the former and quasi Crank Nicolson for the latter). Here we consider 'classic' only the predictor part where a second order Adam Bashforth scheme with modified coefficients is used [33]. It worth to mention that, for the classic pressure correction, in Paravento [33], a third order Adam Bashforth scheme has also been tested for the momentum equations. The original predictor–corrector scheme of Treurniet has been tested as well. In all these cases the same results were obtained and therefore the same numerical difficulties were found [33].

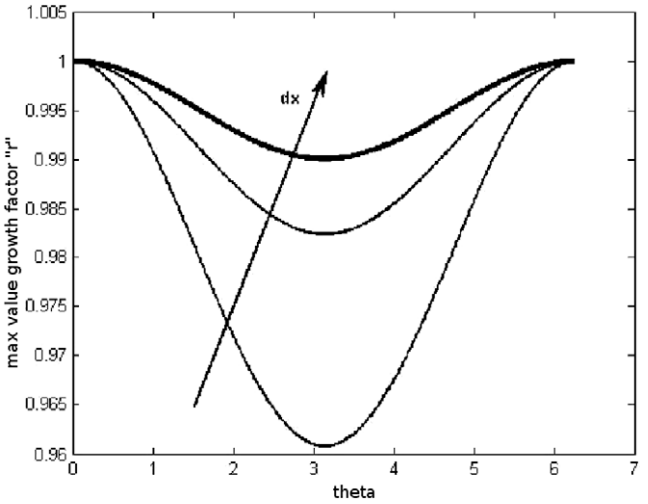

Fig. 8. Behaviour of the error growth factor for IMEX scheme when Δx has values 0.001, 0.0015 and 0.002. The other parameters are $D = 0.01$ and $\epsilon = 0.001$. The time step is taken $\Delta t = 10^{-6}$. The direction of the arrow indicates increasing value of Δx.

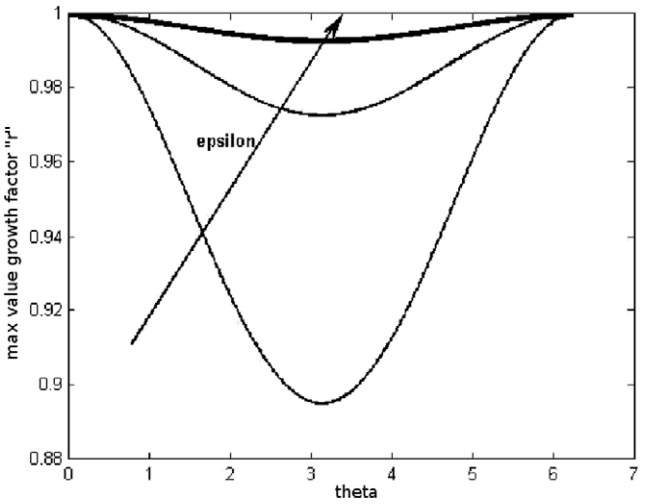

Fig. 9. Behaviour of the error growth factor for IMEX scheme when the source time scale parameter ϵ has values 0.0005, 0.001 and 0.002. The other parameters are $\Delta x = 3s_l\epsilon$ and $D = 0.01$. The time step is taken $\Delta t = 10^{-6}$. The direction of the arrow indicates increasing value of ϵ.

Then, the momentum equations is integrated to an intermediate value $\widehat{\rho u}$,

$$\frac{\widehat{\rho u} - (\rho u)^n}{\Delta t} = \frac{1}{12}[23(A_m + D_m)^n - 16(A_m + D_m)^{n-1} + 5(A_m + D_m)^{n-2}] - \nabla p^n \tag{34}$$

A_m and D_m stand for the advective and the diffusive terms (their spatial discretization is described in Appendix A). Then, with the intermediate level $\widehat{\rho u}$ the pressure correction equation is built:

$$\frac{(\rho u)^{n+1} - \widehat{\rho u}}{\Delta t} = -\nabla p^* \tag{35}$$

where p^* is the pressure correction. Applying the divergence on both sides gives

$$\frac{\nabla \cdot (\rho u)^{n+1} - \nabla \cdot (\widehat{\rho u})}{\Delta t} = -\nabla^2 p^* \tag{36}$$

From the continuity equation the term $\nabla \cdot (\rho u)^{n+1}$ is computed as

$$\nabla \cdot (\rho u)^{n+1} = -\frac{\widehat{\partial \rho}_{n+1}}{\partial t} \tag{37}$$

where the derivative of the density was calculated with Eq. (33).

Now substituting (37) in (36) gives the Poisson equation,

$$\frac{\nabla \cdot \widehat{\rho u} + \frac{\widehat{\partial \rho}^{n+1}}{\partial t}}{\Delta t} = \nabla^2 p^* \tag{38}$$

Eq. (38) is solved with a direct solver based on the Fast Fourier Transform (FFT) algorithm. Once this is solved we can use Eq. (35) to calculate the mass flux at time level $n+1$:

$$(\rho u)^{n+1} = \widehat{\rho u} - \Delta t \nabla p^* \tag{39}$$

And the pressure is updated adding its calculated correction value:

$$p^{n+1} = p^n + p^* \tag{40}$$

The continuity equation can now be integrated to calculate the density at the new time level ρ^{n+1},

$$\frac{\rho^{n+1} - \rho^n}{\Delta t} = \frac{1}{12}[23F^n - 16F^{n-1} + 5F^{n-2}] \tag{41}$$

with $F = \nabla \cdot (\rho u)$ (discretized with central differences). Once the new density value has been calculated we can compute the velocity from the mass flux

$$u^{n+1} = \frac{(\rho u)^{n+1}}{\rho^{n+1}} \tag{42}$$

and the temperature from the equation of state,

$$T^{n+1} = \frac{P_0}{\rho^{n+1}} \tag{43}$$

Finally the G-equation is integrated at the new time level also with a third order Adams–Bashforth scheme

$$G^{n+1} = G^n + \frac{1}{12}\left[23\frac{\partial G^n}{\partial t} - 16\frac{\partial G^{n-1}}{\partial t} + 5\frac{\partial G^{n-2}}{\partial t}\right]\Delta t \tag{44}$$

The details for the spatial discretization of G are contained in Appendix A.

2.3. Reinitialization of the G-equation

To preserve the level set function G as a distance function a so-called reinitialization procedure must be applied. In this work the method proposed by Van der Pijl [30] has been used which we now explain briefly. The reason why we use this method is that it achieves a good conservation of the surface area of the level set during the reinitialization.

Let us consider a general level set equation (in the following G is replaced by the symbol Φ),

$$\frac{\partial \Phi}{\partial t} + U_e \nabla \Phi = 0 \tag{45}$$

The flame position is initialized as the zero level Φ_0 and if Φ is a signed distance function then the evolution of the zero level of Φ represents the flame interface between burnt and unburnt regions evolving in time. For the level set to be a distance function $|\nabla \Phi| = 1$ must hold. Unfortunately during the advection errors are generated and the level set does not necessarily correspond to a distance function anymore. In this case a reinitialization procedure is necessary. One possibility is to apply the algorithm proposed by Sussman [31] by solving

$$\frac{\partial \Phi}{\partial t'} - \mathrm{Sign}(\Phi_0)(1 - |\nabla \Phi|) = 0 \tag{46}$$

for an artificial time t' until a steady state is reached. However, the re-initialized interface can shift considerably with respect to the exact solution. As explained below, the density field around the flame can be influenced by the errors generated during the front propagation and the thermal thickness of the flame can change as well. Van der Pijl has proposed an improved reinitialization method that prescribes a maximum band-width within which the level set is re-defined as a signed distance function:

$$\frac{\Phi^{k+1} - \Phi^k}{\Delta t'} = N_h(\Phi^k, \Phi_0)(1 - q(\Phi_0)) + \frac{\Phi_0 - \Phi^k}{\Delta t'} q(\Phi_0) \tag{47}$$

where N_h is the spatial discretization of $U_e \frac{\partial \Phi}{\partial x}$ and q is a smooth function which defines the band-width,

$$q(\Phi_0) = \exp\left(-\left(\frac{\Phi_0}{\sqrt{\frac{2}{3}(\Delta x^2 + \Delta y^2 + \Delta z^2)}}\right)^2\right) \tag{48}$$

In this study we use a stable third order weighted essentially non-oscillatory (WENO) finite volume scheme [28] for the spatial discretization of $\frac{\partial \Phi}{\partial x}$. This WENO scheme is based on a second order ENO scheme obtained following the approach of Osher and Shu [39]. WENO schemes are central schemes in regions where the solution is smooth but emulates ENO schemes near the singularities of the solution. As Jiang and Peng explain in their revealing paper this is achieved by weighting the substencils of the ENO scheme with the weights adapted to the relative smoothness of the solution of these substencils. The authors tested their WENO scheme by computing the curvature of a level set function. They proved that the WENO scheme is much less noisy and more stable than the ENO scheme. In particular for the WENO scheme the amount of noise stabilizes as the iteration continues due to the fact that WENO smoothly weights the candidate stencils in contrast to the ENO scheme which switches from one stencil to another abruptly even in the smooth part of the solution [28].

2.4. The time step criterion

Due to the low Mach number approximation applied to the flow equations we do not have to resolve the acoustic oscillations. This allows to use a larger time step, Δt, for the numerical integration. Then, the time step depends on the velocity field and the burning speed for the advection part and on the grid resolution for the diffusion part:

$$\Delta t \leqslant \frac{C}{\left|\frac{u}{\Delta x}\right| + \left|\frac{v}{\Delta y}\right| + \left|\frac{w}{\Delta z}\right| + \frac{1}{Re}\left(\frac{1}{\Delta x^2} + \frac{1}{\Delta y^2} + \frac{1}{\Delta z^2}\right) + \left|\frac{s_l}{\min(\Delta x, \Delta y, \Delta z)}\right|} \tag{49}$$

where C is a parameter chosen equal to 0.3.

It is important to note that in our model the characteristic physical time scale, τ_{ph}, is defined by the two quantities, the flame speed s_l and the thickness δ used for the definition of the source term. Considering $\tau_{ph} = \frac{\delta}{s_l}$ then, the largest time step used for the computation must be smaller than τ_{ph} to resolve the physical time scales.

2.5. Smoothing of the total stretch for wrinkled flames

Let us re-write the relation for the flame speed introduced above:

$$s_l = [s_L^0 - s_L^0 L_M \nabla \cdot n + L_M n \cdot (\nabla u) \cdot n] \frac{\rho_u}{\rho} \tag{50}$$

The second and the third terms on the right hand side contain the contribution due to the curvature and the rate of strain. Then we can identify a term that contains the total stretch:

$$K_T = (-s_L^0 L_M \nabla \cdot n + L_M n \cdot (\nabla u) \cdot n) \frac{\rho_u}{\rho} \tag{51}$$

Unfortunately inaccuracies in the computation of the stretch are unavoidable. This is particularly true for the curvature term. As studied recently by Coyajee et al. [32], the order of the error for the curvature term (where the curvature is defined as $\kappa = \nabla \cdot n$) is proportional to $\frac{1}{h}$ with h being the mesh width. In other words, this means that finer the grid larger is the error on the stretch. This can result in dramatic consequences in cases like the interaction of the flame with the recirculation area produced by a body in a flow. One can apply smoothing of the level set function or on the variation of the curvature term.

In this study, at first we have calculated a guessed value of the term containing the total stretch from Eq. (51). Then we have calculated the positions of the intervals Δs along the flame front. This can be done by calculating a narrow band of points around the flame, for instance with the method proposed by Li [35] and then extracting the location of the flame surface. Once we know the location of the flame surface we also know the coordinates of all grid cells that form the flame front. We start to travel from one grid cell to another, on this surface, by using an algorithm that divides the front into curves whose intervals are defined by the minimum distance between two consecutive neighbor grid cells containing the front. The original coordinates of these grid points are stored in an array. The stretch is a scalar defined at the center of each cell and we can use a discrete cubic spline [34] to smooth it (we smooth the term K_T) along the curves we have obtained from the flame surface. Once the stretch on the front has been smoothed we calculate the flame speed from Eq. (50). This process can be eventually iterated in order to have a better evaluation of the normal vectors.

The correct values of the flame speed, s_l, are only those calculated at the position of the interface. However, our zero level set drives a source which is spread over few grid cells and this modifies the density around the zero level and consequently the flame speed around the flame. As demonstrated by Peng [40], it is crucial to extend quantities like the propagation velocity to a neighborhood of the flame along the normal directions at the front. Following Peng we consider the quantity s_l defined on the front and we extend it away from the interface as a constant along the curve normal to the front,

$$\frac{\partial s_l}{\partial t} + \mathrm{Sign}(G) \frac{\nabla G}{|\nabla G|} \cdot \nabla s_l = 0 \tag{52}$$

where $\mathrm{Sign}(G)$ is the sign function of G defined as

$$\mathrm{Sign}(G) = \begin{cases} -1 & \text{if } G < 0 \\ 0 & \text{if } G = 0 \\ 1 & \text{if } G > 0 \end{cases}$$

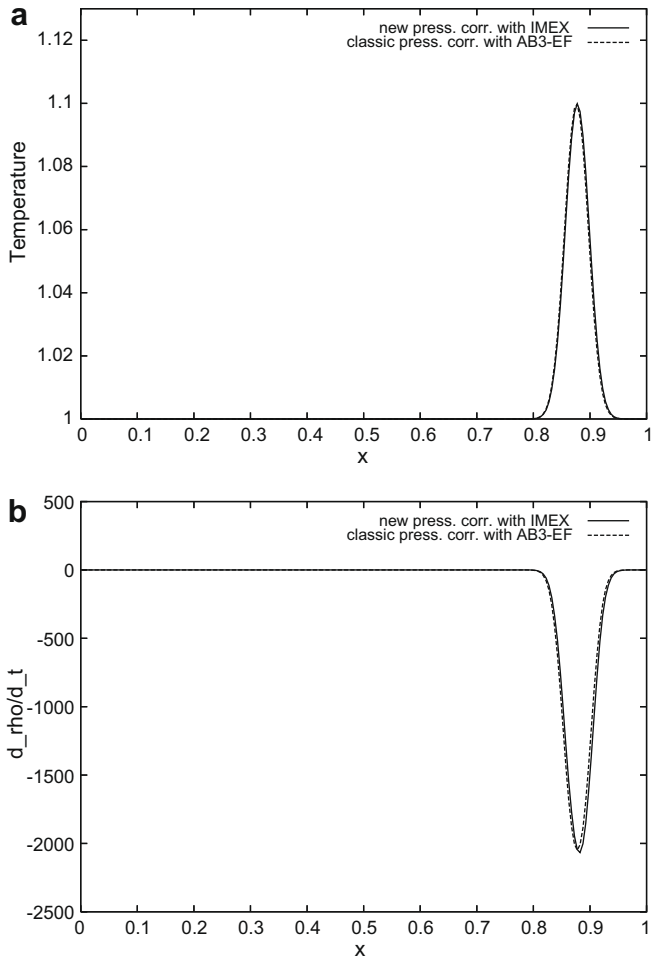

Fig. 10. A flame is ignited in a channel flow and simulated with two approaches for the time integration of the momentum and energy equations. (a) Instantaneous temperature profiles along the channel. (b) Instantaneous $\frac{\partial \rho}{\partial t}$ profile. The density ratio is about 1.1 and the two solutions coincide.

2.6. Comparison with the classic pressure correction

In Section 2.2 we have introduced our pressure correction algorithm and here we are going to compare it with the approach used by Treurniet for the case of a premixed flame. Our approach is in agreement with the statement of Rauwoens [27] mentioning that the two key points in a pressure correction algorithm are the way to determine the density at the new time level and the constraint used to build the Poisson equation. The main difference between the classic scheme and the scheme we have introduced is that in the first case the time derivative of the density is calculated with a backward discretization while in the second case it is computed using the temperature equation and the equation of state. Another important difference in the second case is that the updated value of the density is found by the integration of the continuity equation. In principle more alternatives can be found for this algorithm depending on the correction step. In fact, once the mass flux (or velocity) is calculated in the prediction step (34) then, in the correction step (39) it is corrected to satisfy or the continuity equation or the energy equation or a combination of these two. An interesting study of these algorithms applied to combustion with high density ratios has been done by Rauwoens et al. [27,29]. They have shown the limits of the classic approach in the case of variable density and tested several alternatives. They propose a pressure correction algorithm which contains a Poisson equation with variable coefficients. This equation satisfies a constraint that is a combination of the constraints for continuity and energy. In our case we want to avoid the use of a Poisson equation with variable coefficients because the solvers for this kind of equations are very computationally expensive. As we have seen before in our approach the derivative of the density is calculated from the equation of state and a Poisson equation with constant coefficients is built. Once this is solved we obtain an updated value of the mass flux. Finally, we integrate the continuity equation to advance the density to its final value. This enforces mass conservation.

Now, we want to compute the case of a laminar premixed flame ignited in a channel flow. This is done with both pressure correction algorithms and their results are compared. Let us consider a channel flow with domain of size $1 \times 0.32 \times 0.7$ in x,

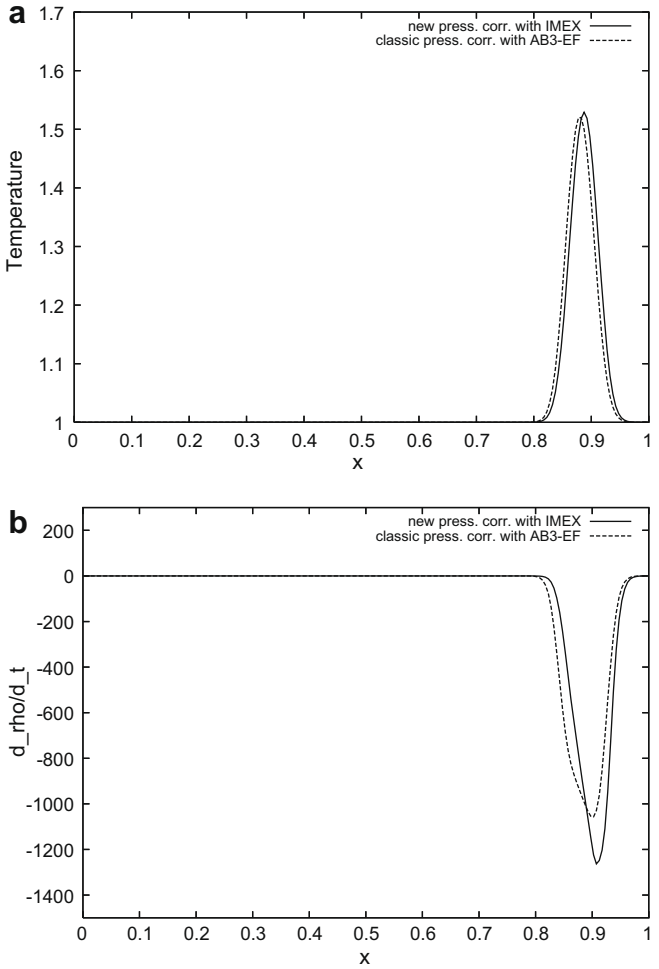

Fig. 11. A flame is ignited in a channel flow and simulated with two approaches for the time integration of the momentum and energy equations. (a) Instantaneous temperature profiles along the channel. (b) Instantaneous $\frac{\partial \rho}{\partial t}$ profile. The density ratio is about 1.55 and the two solutions starts to be different.

y, z directions respectively with number of points $200 \times 64 \times 32$. The inlet velocity is $U = 1$. The outflow condition is determined by imposing zero pressure. No-slip conditions for the velocity are applied at the walls of the domain. The laminar burning speed is $s_l = 1.4$ and the time step is chosen $\Delta t = 10^{-7}$. A laminar flat flame is ignited in the channel where it can develop to its adiabatic condition. The flame normal direction is from the right to the left. We solve the continuity, the momentum, the energy, the equation of state and the G-equation. This test is calculated with two approaches. In the first case we integrate the temperature with AB3-EF and the classic pressure correction is used. In the second case we use IMEX with the new pressure correction. We want to analyze the behaviour of the time derivative of the density when the density ratio increases. If instabilities in this quantity appear then also the solution of the Poisson equation will be influenced. Errors in the calculation of the pressure field propagate through the whole domain hence influencing the velocity field also far away from the discontinuity generated by the flame [27]. Figs. 10–12 show the temperature profiles and the corresponding $\frac{\partial \rho}{\partial t}$ profiles at different instants along the x-center line of the domain. When the density ratio is low (about 1) the two schemes give the same results. When the density ratio approaches the value of two or more the profile of $\frac{\partial \rho}{\partial t}$ for the classic pressure correction scheme starts to deviate from the profile of our scheme until oscillations appear which will produce an exploding calculation.

2.7. Simple flames solution

So far we have described the proposed model based on a combination of a pressure correction algorithm with an IMEX scheme for the time integration of the temperature equation. In this section we want to show that our model is able to retain the main characteristics of laminar flames. We have carried out the calculation of two well known cases: a stabilized 1D flat laminar premixed flame in a channel flow and the influence of the gas expansion on the flame surface. In the first case we

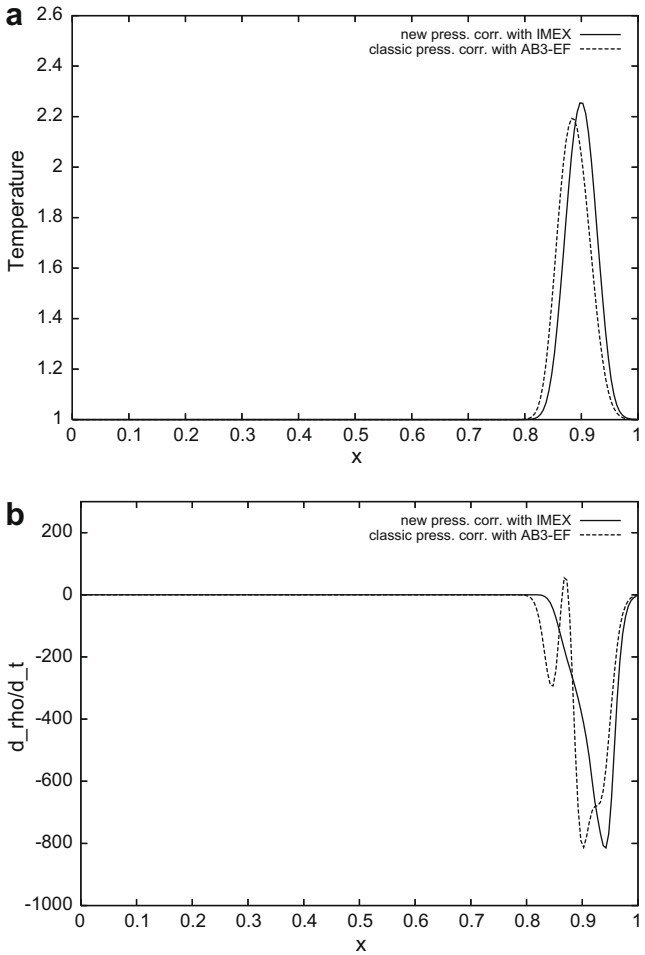

Fig. 12. A flame is ignited in a channel flow and simulated with two approaches for the time integration of the momentum and energy equations. (a) Instantaneous temperature profiles along the channel. (b) Instantaneous $\frac{\partial \rho}{\partial t}$ profile. The density ratio is higher than 2 and the solution with classic pressure correction and AB3-EF scheme starts to diverge.

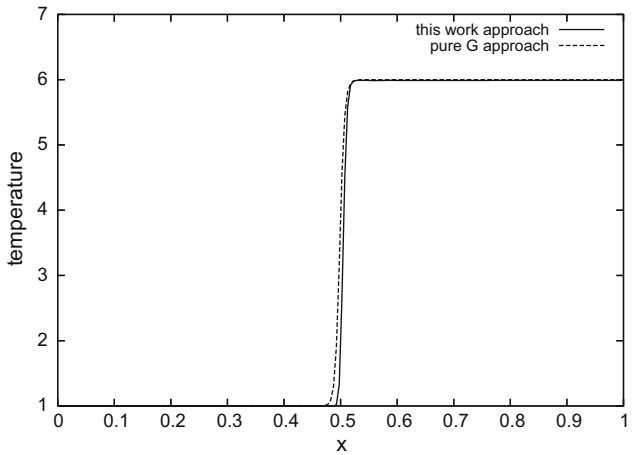

Fig. 13. The temperature profiles for a stabilized 1D laminar flame in a channel flow. Our model is compared with the model by Treurniet [17].

compare our model with that one proposed by Treurniet [17] that is based on a pure *G*-equation model without temperature equation and it uses a classic pressure correction algorithm (implemented in a predictor–corrector fashion) for the time

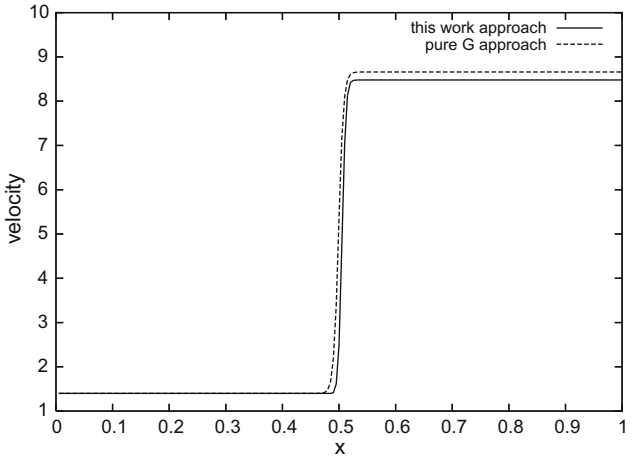

Fig. 14. The velocity profiles for a stabilized 1D laminar flame in a channel flow. Our model is compared with the model by Treurniet [17].

Table 4
Values of velocity and temperature through the flame brush for the Treurniet model.

Position (x)	Velocity	Temperature
0.470	1.406	1.001
0.475	1.423	1.007
0.480	1.480	1.025
0.485	1.664	1.087
0.490	2.188	1.296
0.495	3.399	1.905
0.500	5.366	3.153
0.505	7.158	4.563
0.510	8.111	5.443
0.515	8.478	5.812
0.520	8.602	5.940
0.525	8.641	5.981
0.530	8.654	5.994

integration of the momentum equations. In the second case we reproduce the numerical experiment carried out by Im [45]. This consists of a parametric study of the influence of a small harmonic flow perturbation on the total area of the flame.

2.7.1. 1D laminar flame. Comparisons with a pure G-equation model

Let us consider a 1D channel flow of length $l_x = 1$ discretized with a grid of 200 points. An inflow velocity, U, at the left side of the channel is chosen, while at the outflow a zero pressure condition is applied. A flame is ignited at the center of the domain with normal propagation from the right to the left and laminar burning speed $s_f = 1.4$. A maximum density ratio of 6 is chosen. The flame is stabilized at its initial position by applying an inflow velocity $U = s_f$. We calculate this case with our approach and with the Treurniet model described in [25]. In the latter model there is no energy equation to be solved but a smooth hyperbolic profile of the temperature is imposed at the position of the flame. The spreading of the profile is controlled by a parameter δ_n [25] similar to the diffusive flame thickness δ used in our approach (see Section 1). Both parameters are chosen of the order of a grid cell. In Figs. 13 and 14 the temperature and the velocity profiles for the two models are shown. Our approach allows a steeper jump in the temperature profile. This can also be seen in Tables 4 and 5 which report the positions of the velocity and temperature values through the flame brush. We define the flame brush as the length through the flame where there is a variation of temperature from the 0.1% of T_0 to the 99.9% of T_b with T_0 being the initial temperature and T_b the maximum one. A small difference between the two models is noted for the velocity profiles in the burnt region (Fig. 14). For a stabilized flame conservation of mass must hold at the position of the flame:

$$\rho_u u_u = \rho_b u_b \tag{53}$$

where the subscripts u and b refer to unburnt and burnt regions. Because this is a steady state case the G-equation in 1D becomes

$$u_u \cdot \nabla G = s_f |\nabla G|$$

and because G is a distance function we have

$$u_u = s_f$$

Table 5
Values of velocity and temperature through the flame brush for this thesis model.

Position (x)	Velocity	Temperature
0.490	1.412	1.000
0.495	1.613	1.018
0.500	2.492	1.324
0.505	4.728	2.660
0.510	7.055	4.502
0.515	8.126	5.580
0.520	8.419	5.912
0.525	8.469	5.974
0.530	8.476	5.987
0.535	8.478	5.991

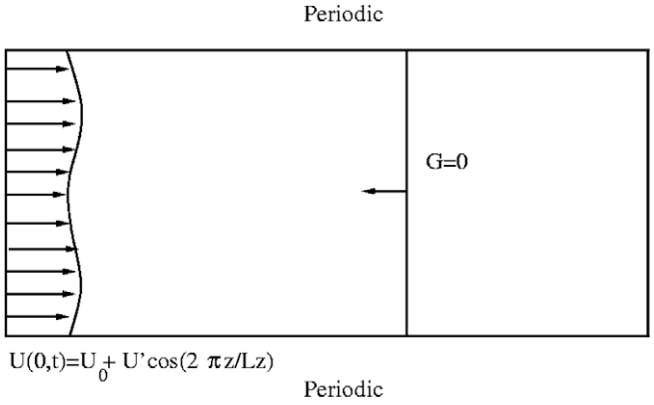

Fig. 15. Configuration of the domain for the numerical experiment performed by Im [45]. The inlet x-velocity consists of an harmonic field. The boundary conditions at the top and the bottom walls and at the outlet are periodic and zero pressure respectively. The flame is ignited at $G = 0$.

By substituting the last relation in (53) and using the equation of state we have

$$u_b = s_f T_b / T_0$$

In this case is $T_0 = 1$ and $T_b = 6$ therefore for the ideal case it is $u_b = 1.4 \times 6 = 8.4$.

Now, by looking at the last row of values in Tables 4 and 5 it is possible to calculate the relative error on the burning velocity u_b for the pure G-approach and for our model. In the first case we find an error of 3% while in the second case an error of 1%. This is because the steeper the temperature profile the closer the flame configuration is to the ideal flat flame.

2.8. Premixed flame with harmonic inlet velocity flow field

The purpose of this section is to check if our model can qualitatively reproduce the influence of the gas expansion on the flame surface. Following the numerical set-up of Im [45] we consider an initially flat flame ignited in a two-dimensional channel flow with a harmonic horizontal velocity at the inlet.

The domain is depicted in Fig. 15. It has dimensions 1×0.7 with number of grid points 300×140 for x- and z-directions respectively. The boundary conditions are periodic at the top and the bottom boundaries for all quantities and zero pressure condition is applied at the outlet of the domain. The initial vertical velocity is zero. The inlet x-velocity profile is

$$u(x = 0) = s_L + u' \cos(2\pi z / l_z) \tag{54}$$

The laminar flame speed is $s_L = 0.4$. The flame is ignited near the outlet of the channel and its position is located where is $G = 0$. The flame moves from the right to the left propagating into the fresh mixture. The Reynolds number based on s_L and l_z is 2000. The heat release parameter is taken $\tau_h = \frac{T_f - T_0}{T_0} = 1$ and the Markstein parameter, L_M, is such that $L_M / l_z = 0.01$. According to Im, the parameter u'/s_l is considered as an indicator of the strength of the turbulence applied on the flame.

In Fig. 16 the ratio of the wrinkled flame surface (A_T) to the initial flat front (A_0), A_T/A_0, is plotted versus different values of the parameter u'/s_L. The data from Im with zero heat release are also reported. These results confirm what was demonstrated theoretically by Cambray and Joulin [46] and numerically by Im [45]: there is a flame speed and flame surface enhancement due to thermal expansion for weak turbulence ($u'/s_L < 1$). Moreover, according to these authors for larger velocity fluctuations (when $u' = O(s_L)$) it is expected that the effect of thermal expansion induced self-wrinkling of the front will be less

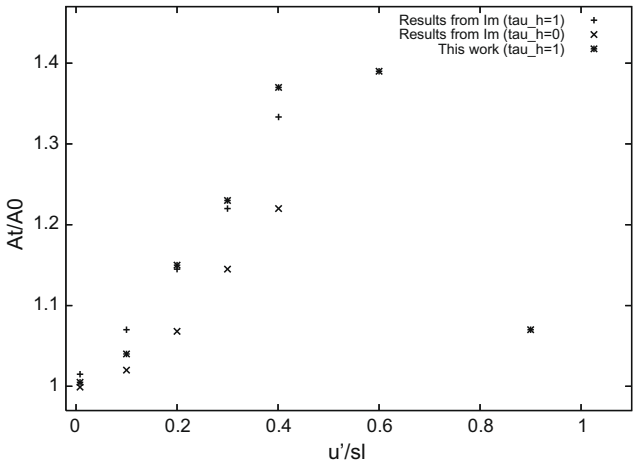

Fig. 16. Ratio A_T/A_0 of the wrinkled flame surface (A_T) to the initial flat front (A_0), A_T/A_0 plotted versus different values of the parameter u'/s_L.

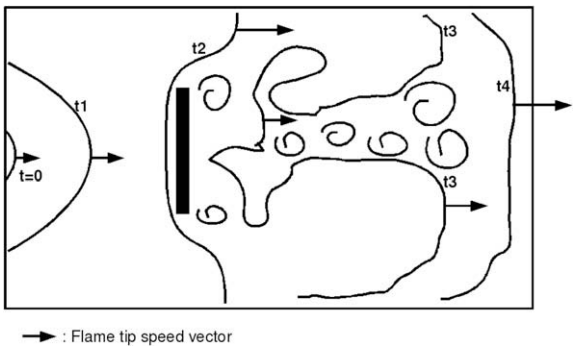

Fig. 17. Evolution of the flame front during deflagration of air–gas mixture in a rectangular domain. At time $t = 0$ the front is ignited as hemispherical surface. At time t_1 the front increases its area with an almost constant velocity of its tip. Afterwards, t_2, the flame has interacted with the obstacle and it propagates through the free space between the body and the walls of the domain with a jet-like behaviour. Since the first instants the flammable flow is accelerated and eddies form at the edges of the obstacle. Once the flame reaches the recirculation zone pockets of fresh fuel are trapped (t_3). After the recirculation zone, t_4, the flame tip speed increases again.

prominent or reduced as the large convective flow field dominates the flame behaviour. However they could not pursue calculations for this case because of numerical difficulties. Our results confirm the theoretical results of Cambray and Joulin. In effect, in Fig. 16 we can see that the enhancement of the flame area does not increase much anymore when the ratio u'/s_L is equal to 0.6, instead it decreases when this quantity approaches 1.

3. Interaction flame-obstacles

We consider the interaction taking place into a rectangular domain filled with a stoichiometric mixture of methane and air. We define the flame tip speed as the speed value of the displacement of the maximum downstream location of the flame front [42]. The domain is semi-confined with solid boundaries on all but one side (outlet). The fuel mixture at rest is ignited by a spark plug at one side of the domain and an initially hemispheric flame front starts to develop (Fig. 17, flame front contour at $t = 0$).

Then, the flame propagates along the domain where an obstacle is set. For this mixture a constant laminar burning speed, s_l, of the unstrained flame front is assumed equal to 0.4 m/s and a density ratio of 6 is considered. It is well understood that if the area of the flame surface increases then also the burning ratio increases. During the interaction flame/obstacle the flame surface is indeed stretched and its area increases. In addition, turbulence in the flammable mixture is produced which can wrinkle the propagating flame front. Therefore, at different times t, several phenomena are observed (an oversimplified sketch of the main steps is given in Fig. 17):

- the flammable gas flow is accelerated and eddies are produced at the edges of the obstacle;
- the interaction with the obstacle enhances the burning rate and hence the flame speed;

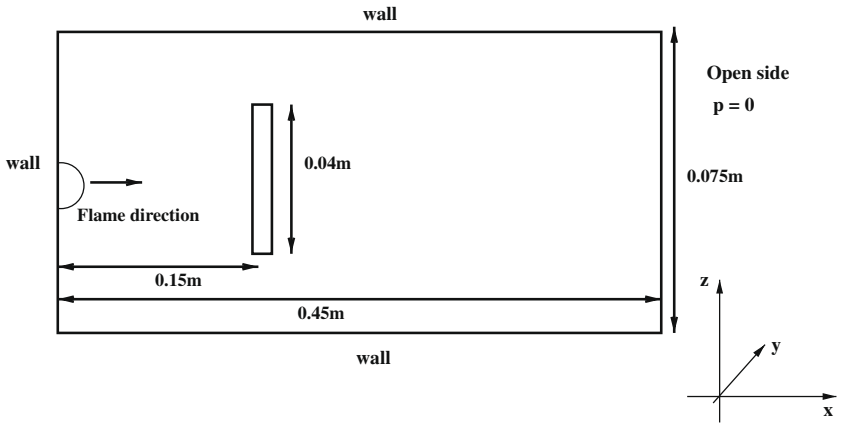

Fig. 18. The geometry used for the cases of a flame interacting with a rectangular cylinder.

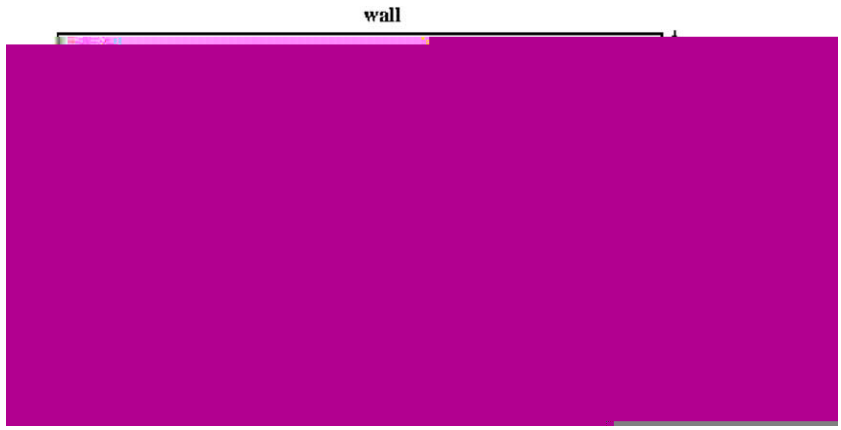

Fig. 19. The geometry used for the cases of a flame interacting with a square cylinder.

- the level of turbulence starts to increase when the flame reaches the obstacle and the turbulence contributes to wrinkle the flame front;
- when the flame reaches the obstacle the pressure reaches a peak;
- the blockage of the channel flow due to the obstacle causes local acceleration of the flame front in the form of jetting;
- in the recirculation zone that is formed behind the body, the flame is wrapped on itself (wake/flame interaction) and the flame speed reduces. Pockets of fuel can be trapped;
- after the recirculation zone the flammable flow velocity and the level of turbulence have raised such that the velocity of the flame front increases again.

We focus on two geometries studied by Ibrahim [2,38], Masri [1] and Hargrave et al. [3]. The first one consists of a rectangular domain of size $0.45 \times 0.15 \times 0.075$ m^3 in x, y, z direction respectively. The domain is closed at the left side where a flame is ignited and open at the right side (Fig. 18).

A sealing membrane at the outlet keeps the gas inside the domain and the bursting time is unknown in the experiment and will not be considered in our simulations. A rectangular cylinder with thickness of 0.012 m and a side 0.04 m is placed with its center line 0.150 m away from the left closed side of the domain. The blockage ratio of the obstacle with respect to the yz-cross-section is 53%. The second geometry differs from the first one only with respect to the shape of the obstacle which is now a square cylinder with a side 0.04 m (Fig. 19).

The first geometry described here was studied numerically by Patel et al. [36] who used a numerical model based on a RANS approach for the solution of the flow field and a flame surface density approach (FSD) for the combustion modeling. With the method described earlier in this paper we present the simulation of these two geometries and a comparison with Patel's results. The flame is ignited as an hemisphere with radius of 5 mm at the center of the left closed side of the domain. No-slip and non-penetration conditions for the velocity are applied at the walls of the channel, zero pressure is set at the outflow and a zero gradient condition is chosen for all scalar quantities at the walls including the temperature. The obstacles

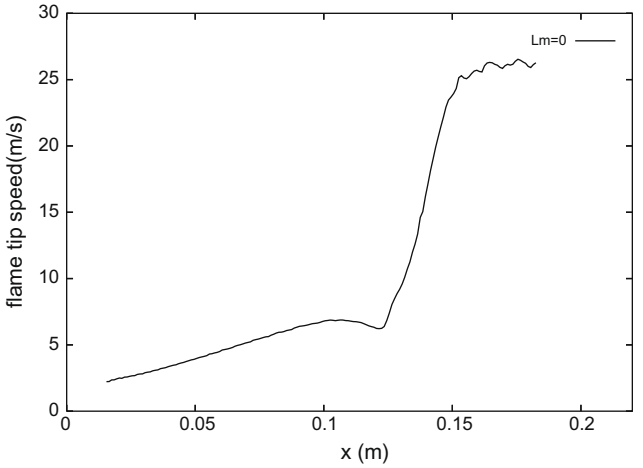

Fig. 20. Flame tip speed profile along the main length of the domain for the case with $L_M = 0$ (no stretch effects). The computation is stopped at the early stage of the interaction with the body.

are considered adiabatic. The Reynolds number is $Re = \frac{\rho_0 s_l l_{z_{body}}}{\mu_0} = 1600$. It is important to underline that the characteristic physical time scale, τ_{ph}, of our model is defined by the laminar burning speed, s_l^0, and the thermal flame thickness, δ_f. Considering, for the first two configurations, $s_l^0 \sim 0.4$ m/s and $\delta_f \sim 0.001$ m it is found $\tau_{ph} = \delta_f / s_l^0 = 0.0024$ s. The largest time step used in the computations is $\sim 10^{-5}$ s therefore the physical time scales are resolved.

3.1. Calculation for the optimization of the diffusion flame thickness δ and the influence of the Markstein parameter L_M

In our approach we apply two types of optimizations. The first optimization is based on numerical experiments: how small can the diffusion parameter δ be such that the front is as steep and thin as possible. The second optimization is physical: diffusion thickness δ and thermal thickness δ_f are linearly related [13] and because during the interaction with an obstacle the thermal thickness changes then also the diffusion thickness can be expected to follow the same trend. We have mentioned earlier that in this study we assume the diffusive parameter of the Gaussian source term (Eq. (11)) to be the diffusive flame thickness δ. In this way the diffusive thickness can be calculated by a relation for the full width at half maximum of the distribution (FWHM):

$$\mathrm{FWHM} = 2\sqrt{2\ln 2}\delta = \frac{\Delta x}{3} \tag{55}$$

where we have set the last equality based on optimization by numerical experiments in order to have a flame as thin as possible (first optimization) while the maximum value of the source term (dependent on δ) is released at each grid cell containing the zero level set. This relationship makes sure that 90% of the source is distributed over a range never less than at least two grid cells. The idea we follow here is to estimate δ_f, Eq. (14), with a first computation by using a constant δ calculated by (55). After this first calculation we know how the profile of δ_f changes, that is the information we could not guess in advance. Then, we can make δ changing with the same trend (the same percentage of change during the propagation) because as we know δ is linearly related to δ_f (second optimization). Moreover, because the Markstein parameter, Eq. (13), is function of δ also L_M needs to be optimized according to the profile of δ_f. In fact, L_M has a direct influence on the flame speed, Eq. (50). From numerical runs we have found that if we use a constant δ during the whole calculation the error on the results is about 5–10% with respect to the experimental data. A better optimization of this parameter is postponed to a future work.

Let us consider the first geometry with a rectangular cylinder as obstacle. A grid of $450 \times 64 \times 150$ points in x, y, z directions respectively is used. The Courant number is $C = 0.3$. Initially the Markstein parameter is set equal to zero ($L_M = 0$) hence no stretch effects on the flame front are included. Let us consider the flame tip speed (that is the quantity measured in the experiments). At each instant the tip is the furthest point of the flame in the main direction of propagation. In Fig. 20 the velocity of the tip is plotted versus the distance from the ignition point and the calculation is stopped at the early stage of the interaction of the flame with the wake behind the obstacle. We can see that the tip speed increases slowly until 0.1 m when a small decrease occurs just before the front reaches the body.

Now let us consider the effect of L_M on the flame tip speed. The Markstein parameter, L_M, is a prefactor for the stretch in the relation for the displacement speed (Eq. (50)). It is of the order of the diffusive flame thickness, δ, and it can be evaluated with the relation (13). By using a maximum density ratio of about 6 between burnt and fresh regions we find that the Markstein parameter is of $O(L_M) = 2\delta$. In Fig. 21 we plot the flame tip speed for different values of L_M.

The larger L_M the higher the value of the tip speed. This is because the contribution of the stretch increases the flame area. The flame tip speed profile is not smooth because once the small semi-spherical initial flame is imposed in the system and its

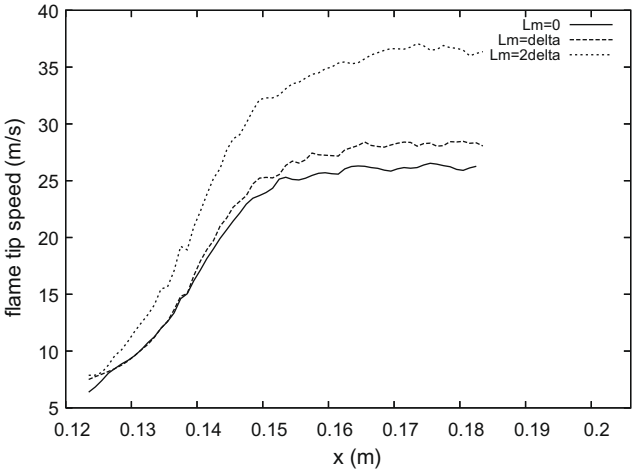

Fig. 21. The flame tip speed for different values of the Markstein parameter L_M.

surface starts to grow during the propagation hydrodynamic instability will make the flame area oscillating and because we extract the instantaneous values of the flame tip in time at all times, then we capture a wiggly profile.

At this point we can run the preliminary calculation that will be used to optimize the profile of δ and L_M with respect to the trend of δ_f. It is assumed $L_M = 2\delta$ where δ is calculated from Eq. (55). In Fig. 22(a) and (b) are plotted versus time the original profile of the thermal thickness, δ_f, and its polynomial fit obtained with a Bezier spline interpolation (over a time-range when the flame is around the position of the obstacle).

It can be seen that δ_f decreases when the flame starts to interact with the obstacle (at a time between 0.025 and 0.03 s). The acceleration of the tip flame can be noted also in Fig. 22(c) where the position of the flame tip in time is shown: at a time of ≈0.025–0.03 s the slope of the curve increases. This is due to the stretching of the flame. It is interesting to note that in the temporal range of about 0.018–0.027 s the flame thickness shows an almost constant profile. This range corresponds to the period of time when the flame is approaching the obstacle and its shape changes: from a spherical shape the front assumes at first a flat shape in front of the object and then, at about 0.03 s it propagates in the space between the block and the walls of the channel.

As discussed earlier, δ and δ_f are linearly related so that after a preliminary computation of the latter a better profile for the former can be found. By using the previous figures it is possible to build Table 6 which gives the percentage variation of the thickness (with respect to its value at $t = 0.02$ s) along the channel.

According to the Clavin and Joulin relation between L_M and δ, L_M should also change in the same way according to the stretching of the flame near the obstacle.[3]

3.2. Grid refinement in the main directions and boundary layer

Now that we have the optimized profile for δ and L_M we can check the influence of the grid refinement on the numerical solution for the first geometry case. The quantity we are interested in is still the flame tip speed. We refine the grid in one direction at a time. In Fig. 23 the flame tip speed is shown for three grid resolutions refined in x-direction: $450 \times 64 \times 150$, $525 \times 64 \times 150$ (16% finer) and $600 \times 64 \times 150$ (33% finer). The results for the finer resolutions in x are close to that one obtained with the coarsest resolution. The flame speed at the relative maximum and minimum points has a difference of less than 2 m/s if we compare the coarsest and the intermediate resolutions and less than 1 m/s if we compare the intermediate and the finest resolutions. This suggests that convergence can be achieved by refinement of the grid. However the computational time increases. For the grid with 450 points in x-direction the computation takes 102,788 CPU seconds (on a AMD 2 GHz processor with 8 GB of RAM), while for the cases with 525 points and 600 points it takes respectively 192% and 259% more time than for the coarsest case. In Fig. 24 we show the case of grid refinement in y-direction (resolutions $275 \times 32 \times 150$, $275 \times 64 \times 150$ and $275 \times 128 \times 150$). Also in this case the computation converges.

Now, we investigate the refinement of the grid in vertical direction, z, and its effect on the boundary layer formed at the top of the rectangular cylinder (the quantities of interest shown below are calculated in the area circled in Fig. 25). We use three grid resolutions refined in z-direction, $300 \times 64 \times 150$, $300 \times 64 \times 210$ and $275 \times 64 \times 300$ points respectively (in these cases the x-length of the domain has been reduced to 0.3 and 0.275 m respectively). The same time step is used: $\Delta t = 6 \cdot 10^{-7}$. In effect, our DNS must have enough points to be able to reproduce the boundary layer that develops around

[3] The following approach can be used to obtain a smooth profile of a quantity in a given interval. Let us assume we have an interval ΔL composed of N points each one indicated by the index i. A quantity q is defined in ΔL with initial value q_0 and final value q_L. Then a profile of $q(i)$ in ΔL can be computed as $q(i) = q_0 \cdot \left[\left(\frac{q_L}{q_0}\right)^{1/N}\right]^i$ with $i = 1, \ldots, N$.

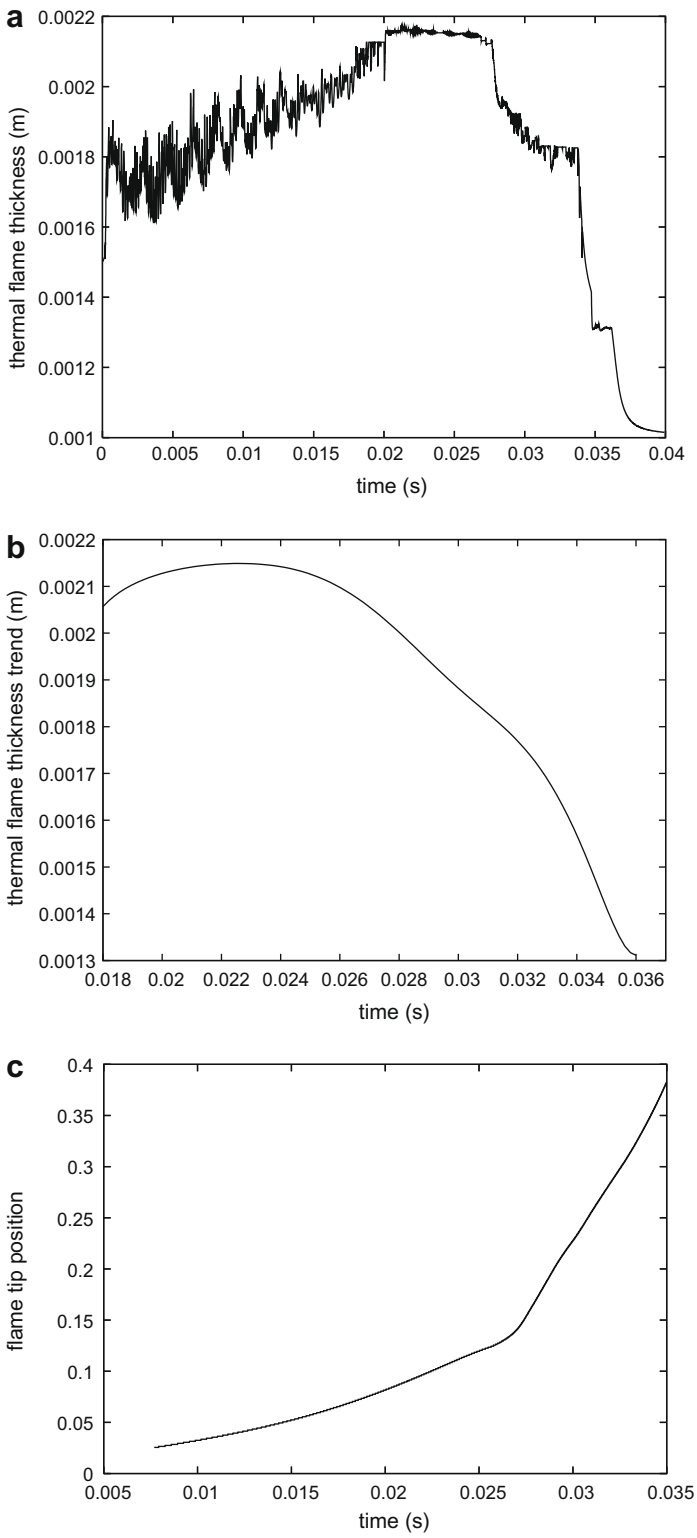

Fig. 22. (a) Thermal thickness versus time for the first calculation. (b) Thermal thickness versus time for the first calculation (polynomial fit over a time-range when the flame is around the position of the obstacle). (c) The position of the flame tip in time.

the obstacle. A first approximation of the boundary layer thickness can be done in the following way. From the previous simulations we know that before the flame interacts with the obstacle its speed slightly decreases and the thermal thickness

Table 6
Variation of the flame thickness along the channel.

x-Intervals along the channel (m)	% Var. of δ_f with respect to δ_f ($t = 0.02$ s)
0.12–0.14	7
0.14–0.28	14
0.28–0.32	15
0.32–0.35	47

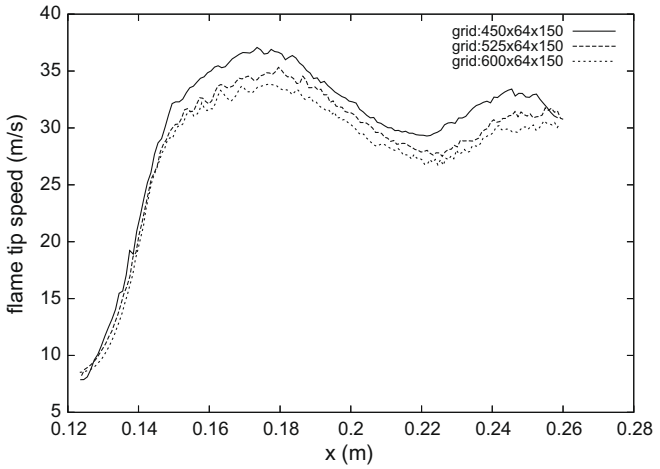

Fig. 23. Calculation of the flame speed for three grid resolutions refined in x-direction in the case of the Ibrahim set-up (rectangular cylinder as obstacle).

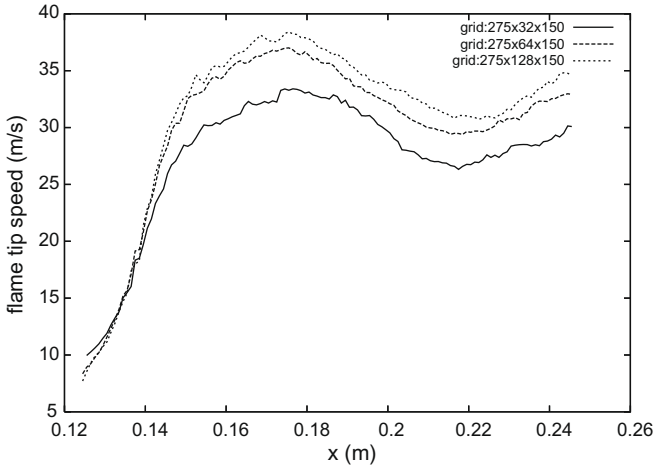

Fig. 24. Calculation of the flame speed for three grid resolutions refined in y-direction in the case of the Ibrahim set-up (rectangular cylinder as obstacle).

assumes an almost constant profile in a short temporal range starting at 0.02 s (Fig. 22(a)). At this instant we take the mean value of the flow velocity (in x-direction), which is about 2.1 m/s, as mean stream velocity U. Then, by means of the Blasius relation we calculate an estimate for the thickness of the boundary layer at the top on the cylinder:

$$\delta_L = \frac{5L}{\sqrt{\frac{UL}{\nu}}} = 0.00122$$

(with L the thickness of the cylinder). The ratio $\frac{\delta_L}{\Delta z}$ for the three grid resolutions is 2.5, 3.3 and 5 respectively. In Fig. 26 we note the convergence of the boundary layer profiles. The finest grid has 6 points in the boundary layer.

Another quantity of interest is the total kinetic energy, k_T. Because we do not have periodic directions in our configuration, we calculate an estimate of this quantity by first averaging the velocity components in the y-direction and then

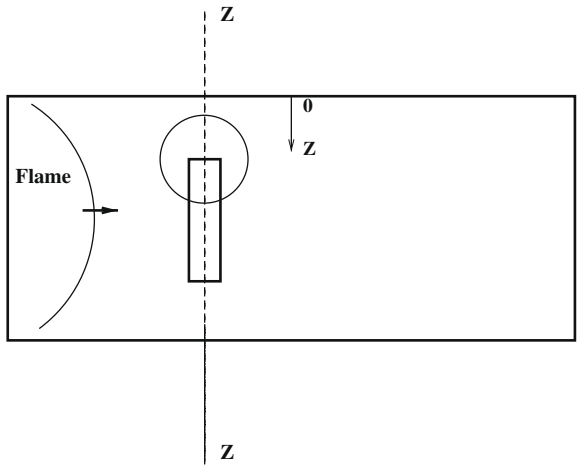

Fig. 25. Set-up for the Ibrahim experiment. The circled area is of interest to analyze the effect of the grid refinement on the boundary layer and other quantities like kinetic energy when the flame approaches and then passes the obstacle.

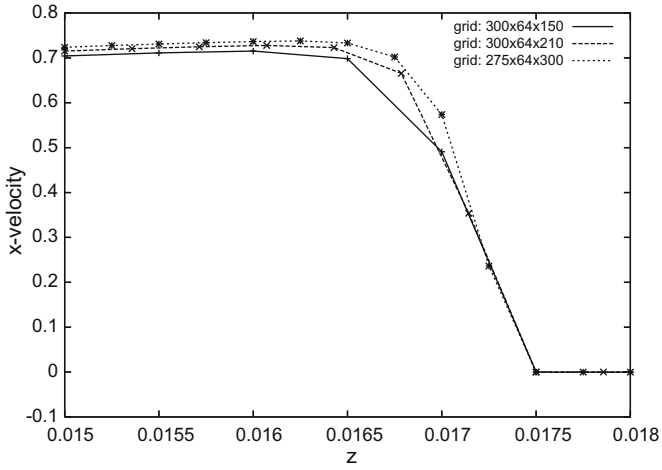

Fig. 26. Boundary layer for different grid resolutions in vertical direction: x-velocity profiles around the top of the cylinder (circled area in Fig. 25).

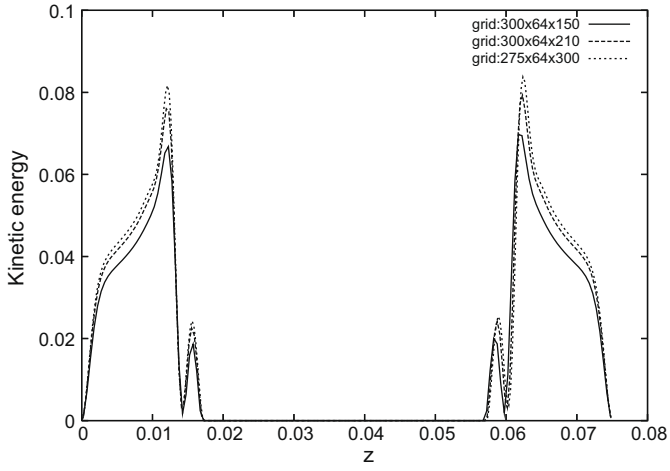

Fig. 27. An estimate of the total kinetic energy ($k_T = \frac{1}{2}\rho(u'^2 + v'^2 + w'^2)$) for the three grid resolutions at an instant $t = 0.004$ s before the flame reaches the body. The profiles are plotted along the z-center line of the body as indicated in Fig. 25.

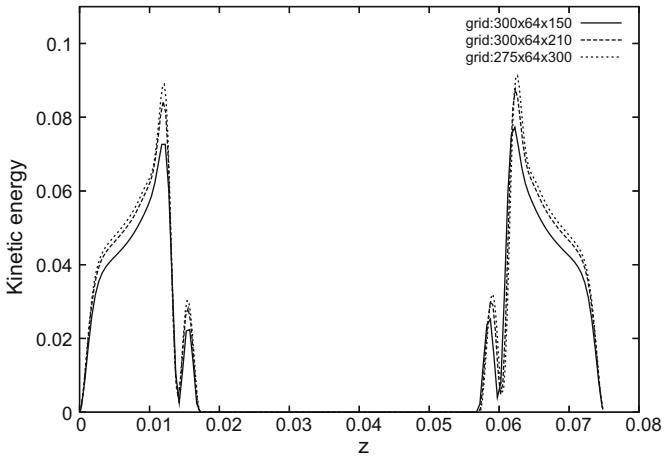

Fig. 28. An estimate of the total kinetic energy ($k_T = \frac{1}{2}\rho(u'^2 + v'^2 + w'^2)$) for the three grid resolutions at an instant $t = 0.024$ s before the flame reaches the body. The profiles are plotted along the z-center line of the body as indicated in Fig. 25.

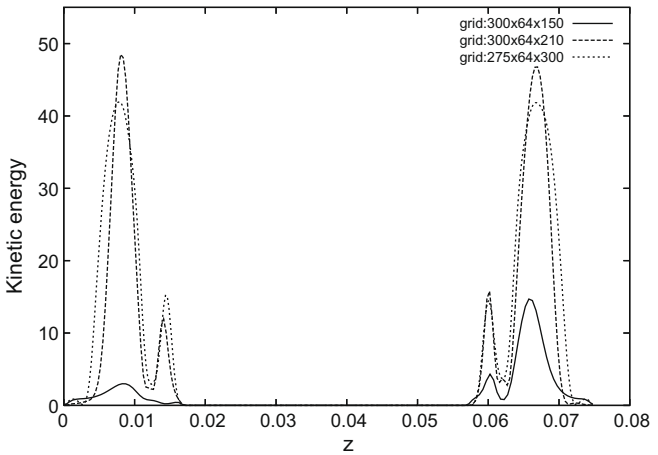

Fig. 29. An estimate of the total kinetic energy ($k_T = \frac{1}{2}\rho(u'^2 + v'^2 + w'^2)$) for the three grid resolutions at $t = 0.03$ s when the flame has reached the body. The profiles are plotted along the z-center line of the body as indicated in Fig. 25. The kinetic energy undergoes a strong increase.

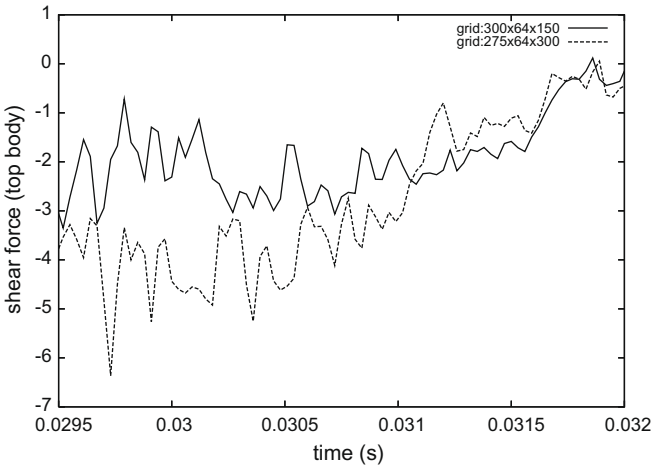

Fig. 30. The normalized force $\frac{F}{\mu} = \int \frac{\partial u}{\partial z} dA$ generated by the shear stress at the top of the body plotted versus time for the finest and coarsest grid resolutions.

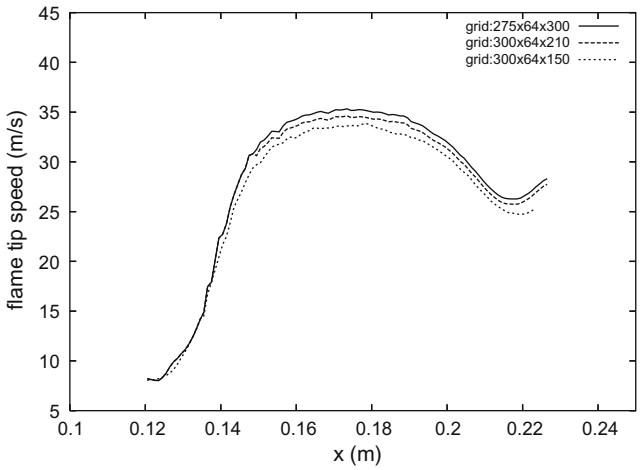

Fig. 31. Calculation of the flame speed for three grid resolutions. The domain is shortened to 0.3 m in x-direction. In the case of the coarsest grid the profile is lower and the recirculation zone is slightly shifted to the right with respect to the other resolutions.

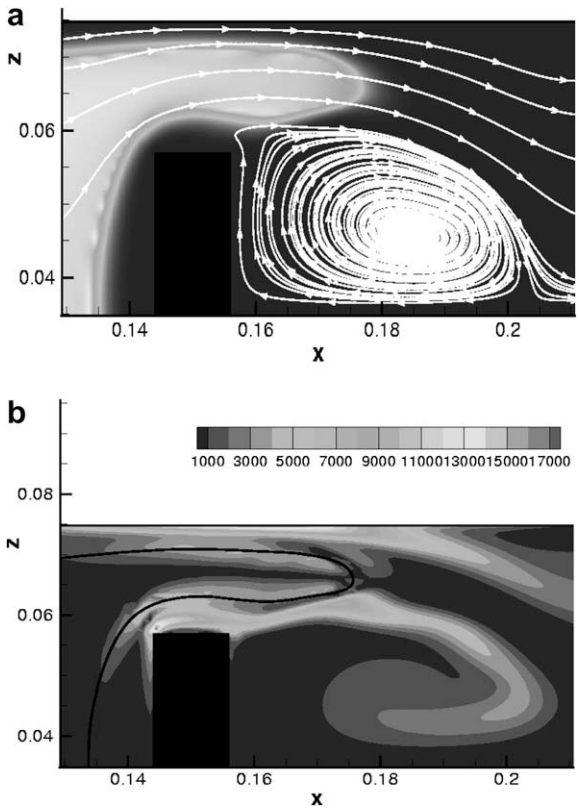

Fig. 32. (a) Temperature isocontour and fluid particles trajectories at the early stages of the interaction of the flame with the body. The picture refers to the zone between the upper part of the body and the wall of the channel. (b) The vorticity modulus and the zero level set plotted at the early stages of the interaction of the flame with the body. The flame position is indicated by the continuous line. This picture refers to the zone between the upper part of the body and the wall of the channel.

subtracting these averages from the instantaneous values to have an estimate of the fluctuating components. In Fig. 27 we show the total kinetic energy for the three grid resolutions before the flame approaches the body (at $t = 0.004$ s).

In Fig. 28 the estimate of the kinetic energy is plotted at the instant $t = 0.024$ s when the flame is close to the body but does not touch it yet. The value of k_T is still small. Fig. 29 shows the instant ($t = 0.03$ s) when the flame is over the body. In this case k_T reaches its maximum value at the top and bottom surface of the body. The flame interacts with the obstacle and

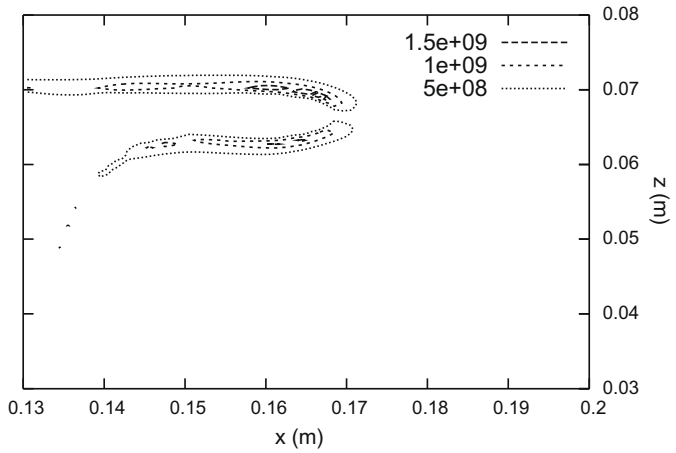

Fig. 33. The maximum absolute values of the baroclinic production term $\left|\nabla\frac{1}{\rho}\times\nabla p\right|$. Vorticity production is maximum when the gradients of the pressure and of the density are not aligned. This is the case along the flame front as shown in this figure.

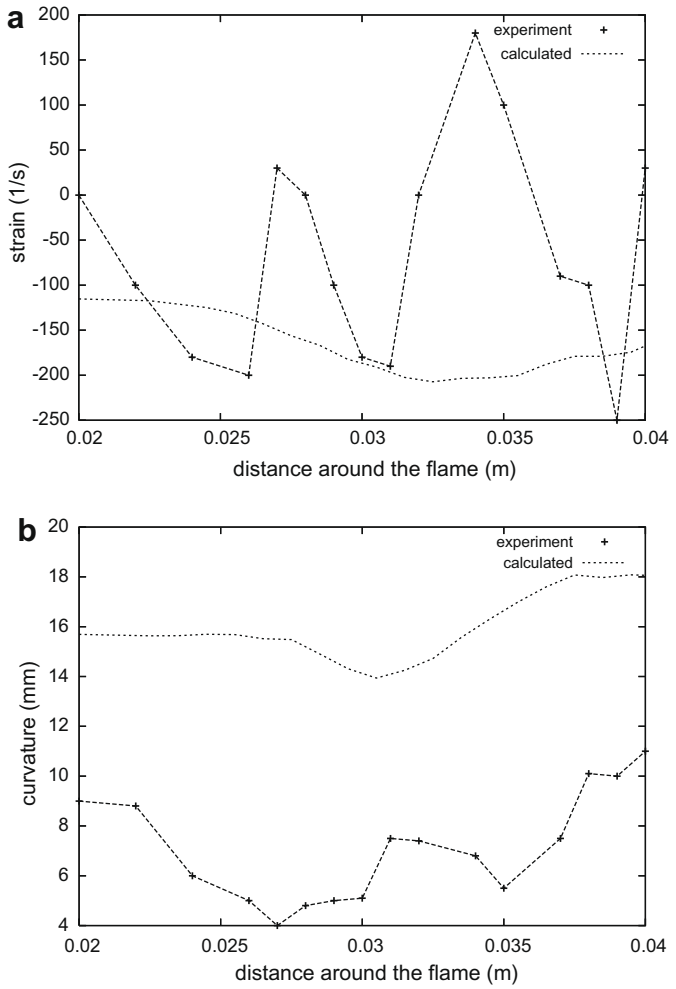

Fig. 34. (a) An instantaneous plot of the strain around the flame (experimental data and calculated profile). The calculated and measured values are not taken at the same time and position therefore this graph is intended for comparing only their orders of magnitude. (b) An instantaneous plot of the radius of curvature around the flame (experimental data and calculated profile). The calculated and measured values are not taken at the same time and position therefore this graph is intended for comparing only their orders of magnitude.

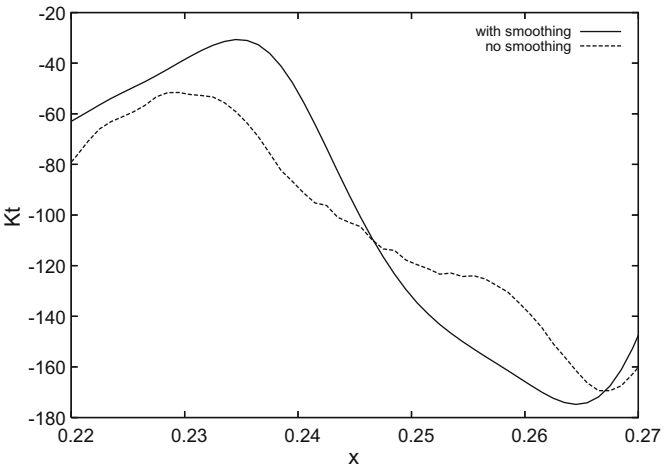

Fig. 35. An instantaneous plot of the total stretch of the flame past the corner of the body in the case with high and low smoothing.

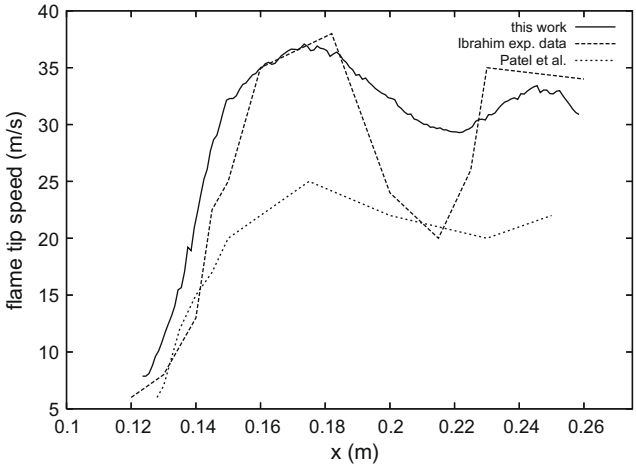

Fig. 36. Flame tip speed comparison with experimental data and numerical calculations.

its propagation starts to be non-symmetric. This effect is prominent for the case of the coarsest grid. This phenomenon is influenced by the 'turbulence' produced during the interaction and in particular we paid attention to the shear stress produced at the top of the body. The shear stress generates a force (F) over the top face (A) of the obstacle. This force, normalized by the viscosity μ is given by $\frac{F}{\mu} = \int \frac{\partial u}{\partial z} dA$. In Fig. 30 this quantity is plotted in time for the finest and the coarsest resolutions. We note a difference in the shear force for the two resolutions in a short time interval around the values $t = 0.03$ when the flame is over the body. In this interval, in the case of the coarsest grid, the absolute value of the shear force is the smallest one. For this resolution one would expect the flow in principle to accelerate more because of the smaller shear. Instead this case presents the lowest peak in the kinetic energy, hence the interaction flame/body is not well captured resulting in a weaker propagation of the flame. In other words, for a poorly resolved boundary layer the stretching of the flame is not reproduced completely and therefore the enhancement of the flame speed, which is related to the increase in flame surface, is less intense.

In Fig. 31 the flame tip speed along the x-direction is plotted. The grid refinement shows converging calculations. Moreover, in the case of coarsest grid the profile is lower and the recirculation zone is slightly shifted to the right.

3.3. Simulation of the Ibrahim and Masri experiments

Once the profiles of δ and L_M have been optimized we calculate the cases of the two geometries described above with rectangular (Ibrahim set-up) and square (Masri set-up) cylinders as obstacles placed in a deflagration tunnel. For the computational results shown in this section we have used a grid with resolution $450 \times 64 \times 150$ points in x, y, z directions respectively. In the case of the Ibrahim set-up at first we analyze the characteristics of the front at the early stage of the

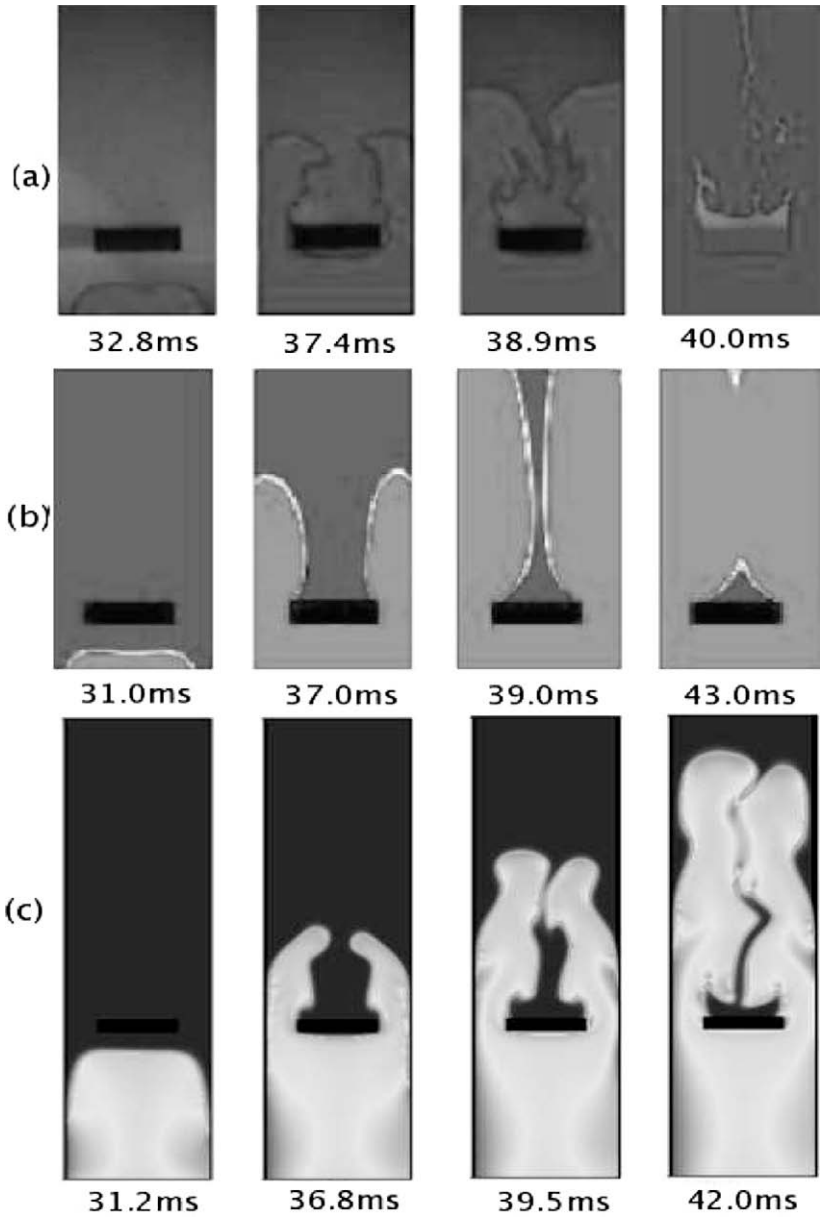

Fig. 37. Temperature isocontours at different instants. (a) Experiment by Ibrahim et al. (b) Calculation by Patel et al. (c) This work calculation (these pictures are not scaled exactly in the same way).

interaction with the wake. In Fig. 32(a) the interaction of the flame front in the wake past the corners of the body is shown by plotting the temperature field with the fluid particles trajectories. This picture is an enlargement of the upper part of the obstacle. A recirculation area is created by the object.

In Fig. 32(b) the modulus of the vorticity ($\sqrt{\omega_x^2 + \omega_y^2 + \omega_z^2}$) is plotted together with the zero G-level. The vorticity decreases at the position of the flame due to the thermal expansion while it increases at the edge of the flame due to the baroclinic production mechanism (Fig. 33).

The vorticity also increases after the body due to the friction of the accelerated flow with the body and the walls.

Hargrave et al. [3] repeated the same experiment of Ibrahim and they used PIV technique to measure the displacement speed, the strain and the curvature terms of the flame front at the early stages of the interaction with the wake formed behind the obstacle. However, these authors report that the measurements close to the walls were inaccurate since the rate of change of the flow velocity was very high with significant variation during the time over which the flame speed was calculated. Moreover, we do not know the exact position and time interval used by Hargrave et al. for taking these measurements.

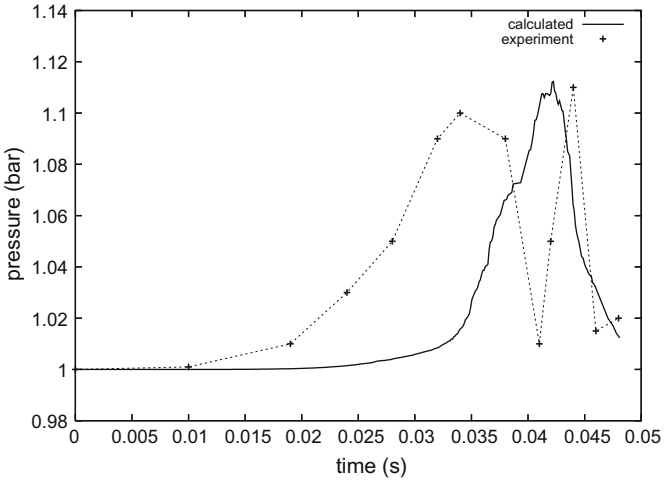

Fig. 38. Comparison of calculated overpressure with experimental data for the interaction flame/rectangular obstacle. The first peak of the experimental results is due to the bursting of the disposable membrane that keeps the gas into the tunnel. This phenomenon is not included in the numerical simulation.

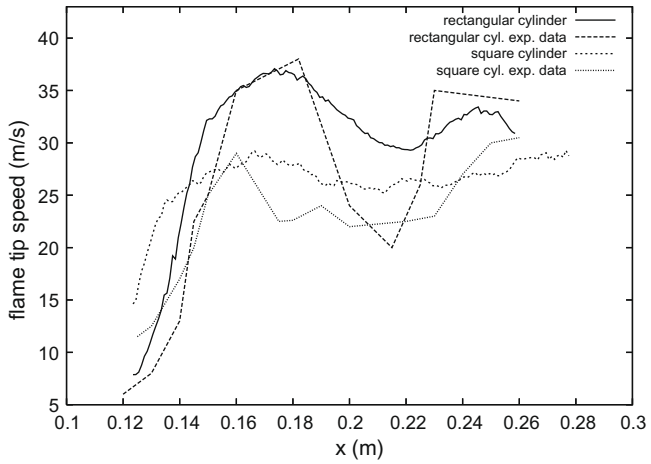

Fig. 39. Comparison of the flame tip speeds between the cases of square and rectangular obstacles. The calculated and the experimental values are shown.

Therefore, here we are only interested in comparing the order of magnitude of calculated instantaneous values of the strain and the curvature terms with the order of magnitude of the experimental results. This comparison is shown in Fig. 34(a) and (b). The values are plotted at an instantaneous position of the flame (different for the calculated and the measured values) over a range of 20 mm.

The calculated values are averaged in the span wise direction y. Despite the fact that the inner flame structure is not resolved and the thermal thickness spreads over a maximum range of about 6–8 cells, their order of magnitude is not too different from the experimental data. In Fig. 35 the total stretch of the front at a certain instant past the corner of the body is also shown. The two profiles correspond to the case with and without smoothing of the stretch. The smoothed profile is obtained with a high level of smoothing (see Duris algorithm, 1980 [34], for more details). The fact that we smooth the stretch means that we redistribute the energy contribution due to the enhancement of the flame surface but still keeping the total surface conserved. The flame tip speed is shown in Fig. 36.

This picture compares our results with the experimental data of Ibrahim (repeated also by Hargrave et al.) and with the simulation of Patel et al. [36] that, at our present knowledge, is currently one of the first attempts of such a calculation (a very recent LES simulation of the same problem has been done by Di Sarli et al. in 2009 [42], but we had not compared yet their results with the ones presented here). In Patel et al. a RANS approach is used with a κ–ε model for the turbulence. For the combustion modeling they use a flame surface density approach (FSD) that assumes the mean rate of reaction as function of a transport equation for the flamelet surface density. Our results are in good agreement with the experiment, the relative maximum value of the flame speed is well predicted and also the part of the profile in the recirculation area

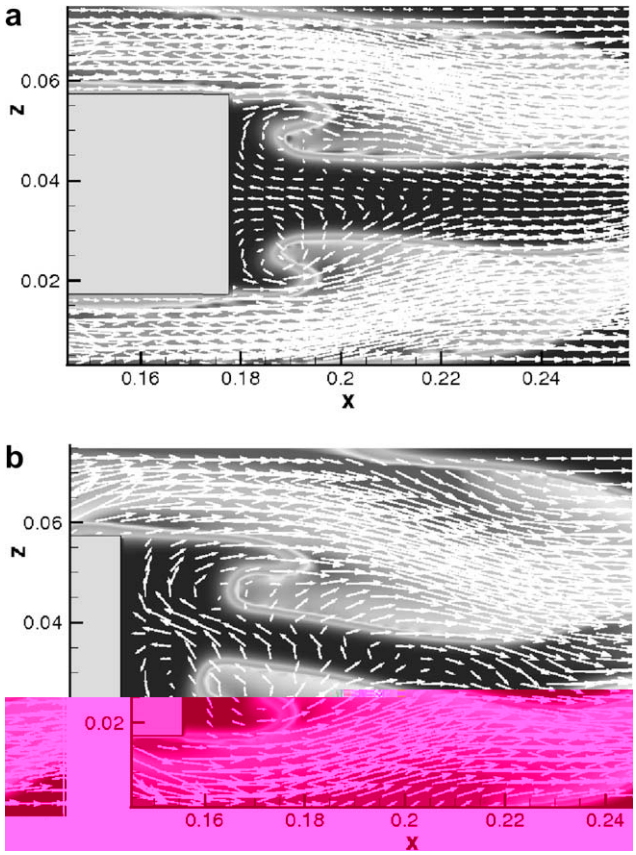

Fig. 40. Particles velocity vectors and flame isocontours for the cases of the square (a) and the rectangular (b) obstacles. For the rectangular cylinder case, the flame front has tendency to wrap more on itself and to trap a larger amount of flammable mixture in the recirculation zone.

is well captured although the minimum in the recirculation area is higher than the experimental data. The isocontours of the temperature (Fig. 37) show that the time evolution of our calculation is qualitatively correct.

In Fig. 38 the overpressure (spatially averaged in the whole domain) calculated in time is shown and compared with the experimental values.

There are two main peaks in the experimental data while in our work we have only one peak predicted. As explained by Patel et al. [36] the first pressure peak is due to the disposable sealing membrane which holds the flammable mixture prior to ignition and insufficient information is available on the time scale of the bursting of this membrane. This effect is not included in our approach. Nevertheless, the predicted peak is close to the second peak in the experiment. Although we have to take into account that when the flame acceleration is such that the local Mach number becomes too large our low Mach number model loses its applicability and the calculated values of the overpressure are questionable.

In Fig. 39 we plot the computed flame tip speed for the first and the second geometries together with the experimental values. The second configuration (square cylinder as obstacle) was studied experimentally by Masri. Hargrave et al. repeated this experiment and measured the flame tip speed. We can see that the calculated profile for the square cylinder is close to the experimental data by Hargrave et al.

We find the same behaviour as Hargrave et al. [3] that for the rectangular body, after the interaction, the flame front undergoes a higher acceleration resulting in a tip speed higher than for the square obstacle. In Fig. 40 we can see that for the rectangular cylinder the flame front has tendency to wrap itself after the body, therefore, trapping more flammable mixture in the recirculation zone with respect to the square cylinder. As explained by Hargrave, this trapped mixture will be rapidly burnt generating more vorticity and a highly wrinkled flame front. This suggests that during the interaction with the flame, the rectangular shape creates more turbulence in the recirculation zone that enhances the flame speed.

4. Conclusions

The main scope of this study has been to introduce a new model for the simulation of low Mach number premixed flames. The energy equation contains a source term which depends on a level set variable (G-equation). The method has been applied in the case of high density ratios between burnt and fresh mixture.

The numerical model is based on a new pressure correction algorithm for the time integration of the flow equations and on an implicit/explicit (IMEX) Runge–Kutta scheme for the energy equation. This approach has proved to be stable for high density ratios and appears a promising tool for further computations of combustion problems.

A second aim has been to simulate the interaction of a premixed flame with obstacles. In particular, we have simulated the experiment performed by Ibrahim and Masri [38] where a flame was ignited in a domain with a rectangular obstacle. The geometry was mimicked with an immersed boundary method (IBM) particularly suitable for the simulation of square and rectangular bodies.

In our model the total stretch is smoothed in order to bound the effects of its numerical error.

The results obtained are very close to the experimental data. The flame tip speed and the interaction of the front in the wake are well predicted. We note that the thermal thickness is reduced due to the interaction with the body. This interaction produces also an overpressure. On the other hand, only if the low Mach number approximation is still valid we can obtain meaningful values of overpressure. In effect, when the local Mach number becomes large the method cannot be applied anymore and one should consider the possibility to rely on a fully compressible model.

Appendix A. Spatial discretization

The spatial discretization (second order finite volume) is outlined here, for pure central differences scheme of the terms A (advection) and D (diffusion) for the x-components of the energy, momentum and G-equations. In the other directions the procedure is similar.

For the energy equation (in non-conservative form) we have:

$$A_T = -\left[\frac{1}{2}(u_{i-1,j,k}+u_{i,j,k})\frac{1}{2}\frac{(T_{i+1,j,k}-T_{i-1,j,k})}{\Delta x_i}\right]$$

$$D_T = \left[\frac{1}{\rho_{i,j,k}}\frac{1}{RePr}\frac{1}{\Delta x_i}\lambda\frac{(T_{i+1,j,k}+T_{i-1,j,k}-2T_{i,j,k})}{\Delta x_i}\right]$$

For the x-component of the momentum considering u as the x-component of the velocity it is:

$$A_m = \nabla\cdot(-u(\rho u))_{i,j,k} = -\frac{u_{i+\frac{1}{2}j,k}(\rho u)_{i+\frac{1}{2}j,k}-u_{i-\frac{1}{2}j,k}(\rho u)_{i-\frac{1}{2}j,k}}{\Delta x h_i} - \frac{v_{i+\frac{1}{2}j,k}(\rho u)_{ij+\frac{1}{2},k}-v_{i+\frac{1}{2}j-1,k}(\rho u)_{ij-\frac{1}{2},k}}{\Delta y_j} - \frac{w_{i+\frac{1}{2}j,k}(\rho u)_{i,j,k+\frac{1}{2}}-w_{i+\frac{1}{2}j,k-1}(\rho u)_{i,j,k-\frac{1}{2}}}{\Delta z_k}$$

$$D_m = \frac{\tau_{xx_{i+\frac{1}{2}j,k}}-\tau_{xx_{i-\frac{1}{2}j,k}}}{\Delta x h_i}+\frac{\tau_{yx_{ij+\frac{1}{2},k}}-\tau_{yx_{ij-\frac{1}{2},k}}}{\Delta y_j}+\frac{\tau_{zx_{ij,k+\frac{1}{2}}}-\tau_{zx_{ij,k-\frac{1}{2}}}}{\Delta z_k}$$

with

$$\tau_{xx_{i+\frac{1}{2}j,k}} = \frac{\mu}{Re}\left(2\frac{u_{i+1,j,k}-u_{i,j,k}}{\Delta x_{i+1}}-\frac{2}{3}\Delta_{i+1,j,k}\right)$$

$$\tau_{yx_{ij+\frac{1}{2}k}} = \frac{\mu}{Re}\left(\frac{u_{ij+1,k}-u_{ij,k}}{\Delta y h_j}+\frac{v_{i+1,j,k}-v_{ij,k}}{\Delta x h_i}\right)$$

$$\tau_{zx_{ij,k+\frac{1}{2}}} = \frac{\mu}{Re}\left(\frac{u_{ij,k+1}-u_{ij,k}}{\Delta z h_k}+\frac{w_{i+1,j,k}-w_{ij,k}}{\Delta x h_i}\right)$$

and

$$\Delta_{ij,k} = \frac{u_{i+1,j,k}-u_{ij,k}}{\Delta x_i}+\frac{v_{ij+1,k}-v_{ij,k}}{\Delta y_j}+\frac{w_{ij,k+1}-w_{ij,k}}{\Delta z_k}$$

For the G-equation there are no diffusion terms, $D=0$. The G-equation is a hyperbolic differential equation with a source term on the right hand side:

$$\frac{\partial G}{\partial t}+u\cdot\nabla G = s_L|\nabla G|$$

At first, it can be re-casted in pure advective form,

$$\frac{\partial G}{\partial t}+u_e\cdot\nabla G = 0$$

with the effective velocity u_e being

$$u_e = u+s_L\cdot n$$

where n is the normal defined in Section 1. The x-component of n on the face of the cell is defined as

$$n_{x_{i,j,k}} = -\frac{\frac{G_{i+1,j,k}-G_{i,j,k}}{\Delta x_i}}{\sqrt{(\nabla G)^2_{i+\frac{1}{2},j,k}}}$$

The term $(\nabla G)^2_{i+\frac{1}{2},j,k}$ must also be calculated on the cell faces. More details can be found in Treurniet [17]. Then, in conservative form the G-equation reads,

$$\frac{\partial G}{\partial t} + \nabla \cdot (u_e G) = (\nabla \cdot u_e) G$$

The flow velocity, u, in the convective term of the G-equation is the local velocity calculated by integration of the momentum equation. The u field and the G field are defined everywhere in the domain. Also the laminar burning speed s_L is defined everywhere in the domain following the approach by Treurniet and before by Candel. A staggered grid is used with u defined at the faces of the numerical grid cells, while $G,\ \rho,\ s_L$ are defined at the center of the grid cells. Because G is defined at the center of the cells, its values and the values of its normal vectors on the cells surface are obtained by interpolation. Also the term $u_e G$ is defined at the cells faces, therefore it is calculated by interpolation by means of a total variance diminishing (TVD) scheme based on WENO scheme [28] while the term on the right hand side of the G-equation is integrated with central differences. The time integration is based on Adams–Bashforth third order.

References

[1] A.R. Masri, S.S. Ibrahim, N. Nehzat, A.R. Green, Experimental study of premixed flame propagation over various solid obstructions, Experimental Thermal and Fluid Science 21 (2000) 109–116.
[2] S.S. Ibrahim, G.K. Hargrave, T.C. Williams, Experimental investigation of flame/solid interactions in turbulent premixed combustion, Experimental Thermal and Fluid Science 24 (2001) 99–106.
[3] G.K. Hargrave, S. Jarvis, T.C. Williams, Experimental investigation of flame/solid interactions in turbulent premixed combustion, Measurement Science and Technology 13 (2002) 1036–1042.
[4] N. Peters, Turbulent Combustion, Cambridge University Press, 2000.
[5] Ronald G. Rehm, Howard R. Baum, The equations of motion for thermally driven. Buoyant Flows, Journal of Research of National Bureau of Standards 83 (1978).
[6] P.A. McMurtry, W.-H. Jou, J.J. Riley, R.W. Metcalfe, Direct numerical simulation of a reactive mixing layer with chemical heat release, AIAA Journal 24 (1986) 962–970.
[7] A. Majda, K.G. Lamb, Simplified Equations for Low Mach Number Combustion with Strong Heat Release, Dynamical Issues in Combustion Theory, Springer-Verlag, 1991.
[8] B. Mller, Low Mach number asymptotics of the Navier–Stokes equations, Journal of Engineering Mathematics 34 (1998) 97–109.
[9] P. Pelce, P. Calvin, Influences of hydrodynamics and diffusion on the stability limits of laminar premixed flames, Journal of Fluid Mechanics 124 (1982) 219.
[10] J. Piana, D. Veynante, S. Candel, T. Poinsot, Direct numerical simulation analysis of the G-equation in premixed combustion, in: J.P. Chollet, P.R. Voke, L. Kleise (Eds.), Direct and Large Eddy Simulation II, Kluwer Academic Publishers, Dordrecht, 1997, pp. 321–330.
[11] T. Poinsot, D. Veynante, Theoretical and Numerical Combustion, R.T. Edwards, 2001.
[12] P. Clavin, G. Joulin, Premixed flames in large scale and high intensity turbulent flow, Journal de Physique Lettres 44 (1983) L1–L12.
[13] R.J. Blint, The relationship of the laminar flame width to flame speed, Combustion Science and Technology 49 (1986) 79–92.
[14] T. Poinsot, T. Echekki, M.G. Mungal, A study of the laminar flame tip and implications for premixed turbulent combustion, Combustion Science and Technology 81 (1992) 45–73.
[15] W.P. Breugem, B.J. Boersma, Direct numerical simulations of turbulent flow over a permeable wall using a direct and a continuum approach, Physics of Fluids 17 (2) (2004) 2005.
[16] F. Paravento, M.J. Pourquie, B.J. Boersma, An immersed boundary method for complex geometry and heat transfer, Flow, Turbulence and Combustion (2007), doi:10.1007/s10494-007-9108-0.
[17] T. Treurniet, Direct Numerical Simulation of Premixed Turbulent Combustion, Ph.D. Thesis, TU Delft, 2002.
[18] E. Lindblad, D.M. Valiev, B. Mller, J. Rantakokko, P. Lotstedt, M.A. Liberman. Implicit–explicit Runge–Kutta method for combustion simulation, in: European Conference on Computational Fluid Dynamics, ECCOMAS CFD, 2006.
[19] R.B. Lowrie, J.E. Morel, Discontinuous Galerkin for Hyperbolic Systems with Stiff Relaxation, Los Alamos National Laboratory, Applied Theoretical and Computational Physics Division, Report LA-UR-99-2517, May, 1999.
[20] L. Pareschi, Central differencing based numerical schemes for hyperbolic conservation laws with relaxation terms, SIAM Journal on Numerical Analysis 39 (4) (2001) 1395–1417.
[21] H.N. Najm, P.S. Wyckoff, O.M. Knio, A semi-implicit numerical scheme for reacting flow, I stiff chemistry, Journal of Computational Physics 143 (1998) 381–402.
[22] J.D. Lambert, Numerical Methods for Ordinary Differential Systems, John Wiley & Sons, 1991.
[23] C. Hirsch, Numerical Computation of Internal and External Flows, John Wiley & Sons, 1988.
[24] L. Pareschi, G. Russo, Stability analysis of implicit–explicit Runge–Kutta schemes for balance laws, 2007, Private communication.
[25] T.C. Treurniet, F.T.M. Nieuwstadt, B.J. Boersma, Direct numerical simulation of homogeneous turbulence in combination with premixed combustion at low Mach number modelled by the G-equation, Journal of Fluid Mechanics 565 (2006) 25–62.
[26] A.J. Chorin, A numerical method for solving incompressible viscous flow problems, Journal of Computational Physics 2 (1976) 12–26.
[27] P. Rauwoens, K. Nerinckx, J. Vierendeels, E. Dick, B. Merci, A stable pressure-correction algorithm for low-speed turbulent combustion simulations, in: ECCOMAS CFD, 2006.
[28] Guang-Shan Jiang, Danping Peng, Weighted ENO schemes for Hamilton–Jacobi equations, SIAM Journal on Scientific Computing 21 (6) (2000) 2126–2143.
[29] P. Rauwoens, J. Vierendeels, B. Merci, A solution for the odd–even decoupling problem in pressure-correction algorithms for variable density flows, Journal of Computational Physics 227 (2007) 79–99.
[30] S.P. Van der Pijl, Computation of Bubbly Flows with a Mass-Conserving Level-set Method, Ph.D. Thesis, TU Delft, 2005.
[31] M. Sussman, E. Fatemi, An efficient, interface-preserving level set redistancing algorithm and its application to interfacial incompressible fluid flow, SIAM Journal on Scientific Computing 20 (4) (1999) 1165–1191.

[32] E.R.A. Coyajee, M. Herrmann, B.J. Boersma, Simulation of dispersed two-phase flow with a coupled volume-of-fluid/level-set method, in: Proceedings of the Summer Program 2004, Center of Turbulence Research, 2004.
[33] F. Paravento, Numerical Simulation of Premixed Flames interacting with Obstacles, Ph.D. Thesis. TU Delft, 2009.
[34] C.S. Duris, Algorithm 547 fortran routines for discrete cubic spline interpolation and smoothing [E1], [E3], ACM Transactions on Mathematical Software 6 (1) (1980) 92–103.
[35] Chunming Li, Chenyang Xu, Changfeng Gui, Martin D. Fox, Level set evolution without re-initialization: a new variational formulation, in: IEEE Proceedings of CVPR, 2005.
[36] S.N.D.H. Patel, S.S. Ibrahim, M.A. Yehia, Flamelet surface density modelling of turbulent deflagrating flames in vented explosions, Journal of Loss Prevention in the Process Industries 16 (2003) 451–455.
[37] D. Veynante, L. Vervisch, Turbulent combustion modeling, Progress in Energy and Combustion Science 28 (2002) 193–266.
[38] S.S. Ibrahim, A.R. Masri, The effects of obstructions on overpressure resulting from premixed flame deflagration, Journal of Loss Prevention in the Process Industries 14 (3) (2001) 213–221.
[39] S. Osher, C.-W. Shu, High-order essentially non-oscillatory schemes for Hamilton–Jacobi equations, Journal of Numerical Analysis 28 (1991) 907–922.
[40] D. Peng, B. Merriman, S. Osher, H. Zhaoand, M. Kang, A PDE-based fast local level set method, Journal of Computational Physics 155 (1999) 410–438.
[41] J.D. Buckmaster, G.S.S Ludford, Lectures on Mathematical Combustion, CBMS-NSF Regional Conference Series in Applied Mathematics, Society for Industrial and Applied Mathematics, 1983.
[42] V. Di Sarli, A. Di Benedetto, G. Russo, S. Jarvis, E.J. Long, G.K. Hargrave, Large Eddy simulation and PIV measurements of unsteady premixed flames accelerated by obstacles, Flow, Turbulence and Combustion 83 (2009) 227–250.
[43] M. Matalon, B.J. Matkowsky, Flames as gasdynamic discontinuities, Journal of Fluid Mechanics 124 (November) (1982) 239–259.
[44] H. Pitsch, A consistent level set formulation for large-eddy simulation of premixed turbulent combustion, Combustion and Flame 143 (2005) 587–598.
[45] H.G. Im, T.S. Lund, J.H. Ferziger, Study of turbulent premixed flame propagation using a laminar flamelet model. Annual Research Briefs 1995, 347-360. Center for Turbulence Research, Stanford, 1995.
[46] P. Cambray, G. Joulin, On moderately-forced premixed flames, in: Twenty-Fourth Symposium (International) on Combustion, The Combustion Institute, 1992, pp. 61–67.